Selection of suitable sub-models for improved confidence in lumped parameter internal ballistic codes

KYA Alzannan

orcid.org/0000-0001-5485-3760

Dissertation submitted in partial fulfilment of the requirements for the degree *Master of Science in Mechanical Engineering* at the North-West University

Supervisor: Prof WL den Heijer

Graduation: October 2019

Student number: 27360016

Dedication

I wholeheartedly dedicate this dissertation to my beloved parents who have been my source of inspiration and strength throughout my life journey. They dedicate their life to support and inspire me. My love and gratitude to them can never be quantified. I also dedicate this dissertation to my parents-in-law who have been encouraging me throughout this journey. I also would like to dedicate this paper to my brothers and sisters who shared their advice and encouragement throughout this journey.

Finally, I dedicate this dissertation to my beloved wife, Munirah, who has been there for me, who sacrifice two years of her educational life just to be with me, and support me by continually providing moral, emotional, and spiritual support. My love and appreciation to her can never be measured. I also dedicate this paper to my beloved son, Yahya, and my beloved daughter, Maria, who gave me the ultimate courage by just being with me.

Acknowledgment

First and foremost, I sincerely express my greatest gratitude to my Creator for giving me this opportunity. I am sincerely grateful to Him for giving me the guidance, strength and encouragement during the challenging moments in completing this dissertation. I am also grateful to Him for His love and kindness.

Secondly, I express my gratitude and sincere thanks to my technical supervisor, Mr. Victor Schabort. Without his guidance and invaluable knowledge, this study will not have been possible.

I also would like to extend my gratitude to the director of the School of Mechanical Engineering and my academic supervisor, Prof. Willem Den Heijer, for his support and guidance.

Abstract

Gun systems manufacturers, propellant manufacturers, ballisticians, and the users of gun systems heavily rely on interior ballistic simulations to describe projectile behavior from the initial point of propellant ignition until the projectile leaves the gun muzzle. The simulation of interior ballistics plays a significant role in optimizing the overall ballistic system, control changes, associated cost, and the minimization of related risks. One of the most commonly used models to simulate the interior ballistic cycle is the lumped parameter model for interior ballistics. The North Atlantic Treaty Organization (NATO) has standardized a lumped parameter model that is known as STANAG 4367 (Moreno, 2009). However, during work routines, it is noticed that when the lumped parameter model of STANAG 4367 is used to simulate a 155 mm artillery system, it predicts the muzzle velocity and maximum chamber pressure of 155 mm artillery system with relatively high deviation. The problem is found to be with the heat transfer model of STANAG 4367.

The primary aim of this research is to find a better alternative to the heat transfer model of STANAG 4367 that is more suitable for simulating a 155 mm artillery system. This research also aims to develop a practical interior ballistic simulation program to be used in different applications of interior ballistics. It also aims to provide guidelines for interior ballistic simulation procedures when the ballistic system has a constant or variable gun wall thickness.

Keywords: Internal ballistic, Heat transfer, Ballistic, STANAG 4367, Nordheim coefficient, Internal ballistic simulation, 155 mm artillery system, Propellant burn rate, Lawton’s coefficient, Gough’s coefficient.

LIST OF ABBREVIATIONS

DAQ	Data Acquisition
DBP	Double Base Propellant
IB	Interior Ballistics
IB0D	Interior Ballistic 0-Dimentional Model
IB1D	Interior Ballistic 1-Dimentional Model
IB2D	Interior Ballistic 2-Dimentional Model
LPM	Lumped Parameter Model
mm	Millimeters
NATO	North Atlantic Treaty Organization
RDM	Rheinmetall Denel Munition
SBP	Single Base Propellant
STANAG	Standardization Agreement
TBP	Triple Base Propellant
WMA	Weighted Moving Average

LIST OF SYMBOLS

A	Area of base of projectile including appropriate portion of rotating band
A_{br}	Area of breech face
A_w	Chamber wall area plus area of gun tube wall exposed to propellant gases
b_i	Covolume of i^{th} propellant
b_I	Covolume of igniter
C	Initial total mass of propellant
C_{gas}	Mass of propellant gas
C_I	Initial mass of igniter
$\overline{C_p}$	Specific heat at constant pressure of propellant gas
C_{pw}	Heat capacity of steel of chamber wall
C_{solid}	Mass of solid propellant grains
C_T	Total mass of propellants and igniter
C_v	The mixture specific heat at constant volume
D	Propellant grain diameter
d	Propellant gas travel distance
D_b	Diameter of bore
DG	Diameter of lands
DL	Diameter of groove
$d(t)$	Grain’s diameter during burning at certain time
D_w	Chamber wall thickness heated
E_{br}	Energy loss due to friction and engraving of the rotating band
E_{exp}	Expansion number

E_d	Energy loss due to air pushed out in front of the projectile
E_{gas}	Gas internal energy at any given moment
E_{gas0}	System total initial internal energy contained in the gas
E_h	Energy lost due to heat transfer to the chamber and barrel walls
E_p	Energy loss due to propellant gas and unburned propellant motion
E_{Pr}	Energy loss due to projectile rotation
E_{Pt}	Energy consumed due to projectile translation
E_r	Energy loss due to recoil
fD	The amount of propellant remaining at any time
F_i	Force per unit mass of i^{th} propellant
F'_i	Adjusted force per unit mass of i^{th} propellant
F_I	Force per unit mass of ignited propellant
f_r	Down-tube resistance factor
f_{FT}	Force temperature factor
$f_{\beta T}$	Burn rate temperature factor
f_β	Burn rate factor
GLR	Groove to land width ratio
h	Heat transfer coefficient of Nordheim, Soodak, and Nordheim
h_0	Free convective heat transfer coefficient for air in gun tube
$h1$	Convective heat transfer coefficient of propellant gas
$h2$	Convective heat transfer coefficient of chamber wall
k	Heat Conductivity of the gun
k_{gas}	Gas Thermal conductivity
L	Grain length
l	Characteristics gas travel length

L_b	Barrel length
l_c	Chamber length
M	Mach number of the projectile with respect to the air
m_p	Mass of projectile
m_{rp}	Mass of recoiling parts
m_g	Gas mass
n	Number of propellants
$\bar{P}$	Space-mean pressure
P_a	Pressure in the ambient air
P_b	Pressure on base of projectile
P_g	Air pressure in front of the projectile
P_0	The breech pressure
P_R	Resistive pressure of the bore due to friction and engraving
P_r	Prandtl number
P'_R	Adjusted resistive pressure of the bore due to friction and engraving
Q	The rate of heat transfer
R	The universal gas constant
r	Burning rate of the propellant
R_e	Reynolds number
S	Surface area of propellant grain
T	Mean temperature of propellant gases
t	Time
T_c	Temperature of chamber wall
T_i	The absolute temperature
t_r	Recoil time
t_{r_0}	Time of the beginning of recoil motion

T_W	Twist of rifling
T_{0i}	Adiabatic flame temperature of i^{th} propellant
T_{0I}	Adiabatic flame temperature of ignited propellant
T_{0_W}	Initial temperature of chamber wall
u	Propellant gas velocity
u_{base}	The gas velocity at the base of the projectile
V	Propellant grain volume
$\bar{v}$	Mean gas velocity
V_c	Volume behind projectile available for propellant gas
V_g	Initial volume of the propellant grain
V_m	Muzzle velocity
v_p	Mass of the projectile
v_{rp}	Velocity of recoiling parts in the earth reference frame
V_{P_i}	Volume of parasitics associated with i^{th} propellant
V_s	The volume occupied by propellant gas
V_0	Volume of empty cannon chamber
x	Travel of projectile
x_{rp}	The displacement of the gun due to recoiling
$\dot{Z}$	Mass fraction burning rate of the propellant grain
Z	Fraction of mass burned of the propellant
α	Burn rate exponent of the propellant
α_a	Ratio of specific heats for air
β	Burn rate coefficient for propellant
ε	Ballistic mass ratio
γ	Ratio of specific heats for propellant gas

γ_i	Ratio of specific heats for i^{th} propellant
γ_I	Ratio of specific heats for igniter
ρ	Propellant gas density
ρ_i	Density of i^{th} propellant
$\bar{\rho}$	Mean gas density
ρ_w	Density of chamber wall steel
λ	Nordheim friction factor
μ	Propellant gas dynamic viscosity

TABLE OF CONTENTS

TABLE OF FIGURES

TABLE OF TABLES

Chapter I Introduction

1.1 Background

Ballistics is an ancient field, which started with spears, slingshots, bows and arrows in historical times. In the 12th century, the Chinese discovered black powder, which is a flammable and highly energetic chemical substance. It consists of potassium nitrates (KNO_3), sulphur (S), and charcoal. By the end of the 13th century, black powder was introduced as a chemical propelling charge where it was ignited to propel a projectile through the barrel of a gun. This was a turning point of the entire field of ballistics. It resulted in the existence of new subfields of ballistics (Gunpowder, 2019).

Today, ballistics can be divided into four major disciplines, which are interior ballistics (IB), intermediate ballistics, exterior ballistics, and terminal ballistics. Interior ballistics is the field of study that focuses on the behavior of the gun, the propelling charge, and the projectile from ignition of the propelling charge to the point in time when the projectile exits the gun muzzle. Intermediate ballistics focuses on the behavior of the projectile during the initial motion as it exits the muzzle. Exterior ballistics, conversely, focuses on the flying behavior of the projectile from muzzle exit until impact. Terminal ballistics covers all the aspects after the projectile hits the target. However, this research will only focus on interior ballistics whilst exterior, intermediate and terminal ballistics will not be included in the scope of this research. As was mentioned, interior ballistics covers all the aspects that commences with the ignition of the propelling charge to the point in time when the projectile exits the gun muzzle. The propelling charge, gun, and projectile are sub-systems of a ballistic system (Carlucci, 2007).

1.1.1 Ballistic system

Figure 1 illustrates the sub-systems and the internal layout of a typical ballistic system.

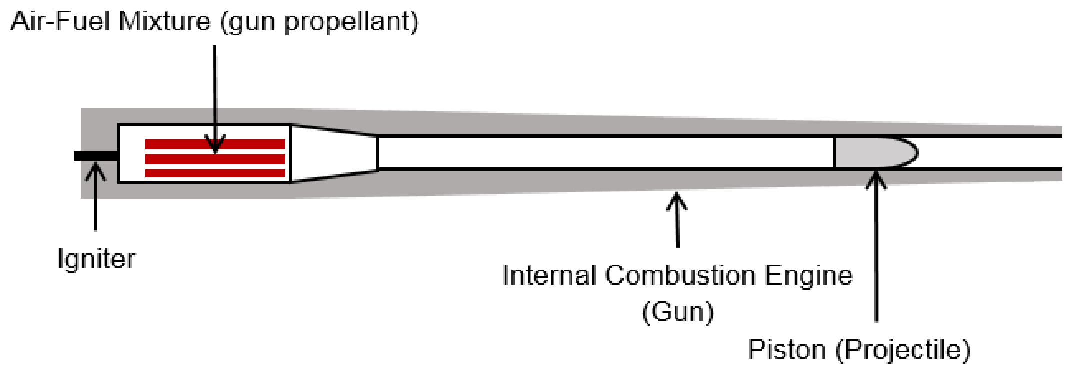

Figure 1: Ballistic system sub-systems and layout

A loaded ballistic system consists of a gun, projectile, igniter, and a propelling charge. The gun can be compared to a single-stroke, internal combustion engine where the projectile is in essence the engine's piston. The propelling charge represents the combusting air-fuel mixture. The propelling charge is a granular chemical substance. The propelling charge is ignited by the igniter and rapidly combusts. The propelling charge consequently transforms into hot expanding gases that contain a significant amount of energy. Rapid pressure buildup consequently occurs inside the gun, followed by a rapid high-pressure gas expansion (Carlucci, 2007). This propels the projectile forward within the gun barrel. Each of the above-mentioned sub-systems are described in more detail in the sections that follow.

1.1.1.1 Gun

A gun consists of a barrel, chamber, and breech or breechblock as illustrated in Figure 2. A gun barrel is typically a metallic tube through which the projectile travels. The front-end of the barrel, through which the projectile discharges, is known as the muzzle. The interior of the barrel is known as the bore. The bore can be either smooth or rifled. The smooth-bore barrel has a smooth interior surface, whilst the rifled-bore barrel has circumferential grooves to induce controlled rotation on the projectile. The back-end of the barrel is attached to the chamber's front-end. Normally, the chamber has a larger diameter than the bore to accommodate the propelling charge. Thus, the chamber diameter is reduced down to the bore diameter through a forcing cone as illustrated in Figure 2. The main mission of the forcing cone is to direct the projectile into the bore. However, it is also found, in some instances, that the chamber has the same diameter as the bore with no forcing cone in between. The chamber's back-end is sealed by means of a breechblock. The barrel, chamber, and breech are manufactured of high-strength metal to withstand the rapid combustion of the propelling charge, as well as the rapid expansion of its high-pressure gases. Figure 2 provides an example of a smooth-bore gun and rifled-bore gun.

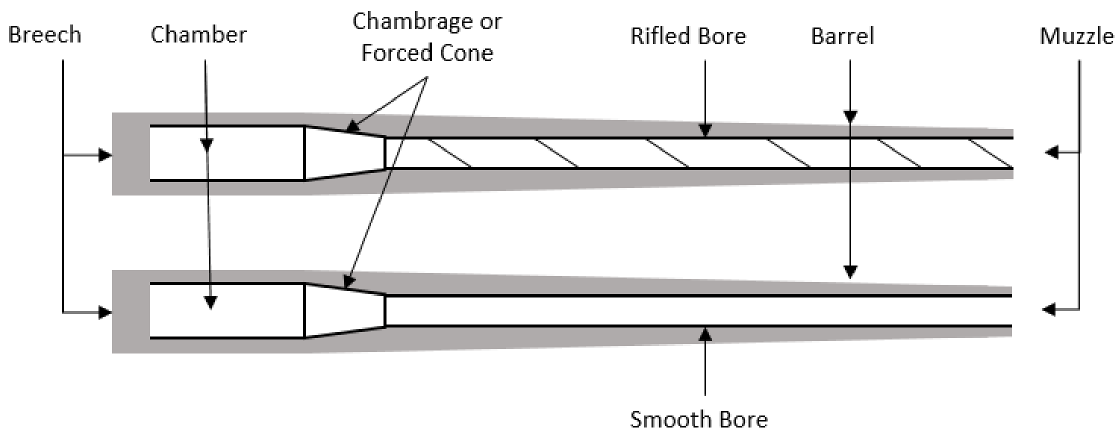

Figure 2: Rifled- and smooth-bore gun

1.1.1.2 Propelling charge

There is a misconception between propelling charges and explosives. Although they are from the same family of energetic materials, there are notable differences. There are two fundamental differences between propelling charges and explosives. Explosives detonate due to shockwaves. Thus, explosives are uncontrollable and they produce a destructive force when they detonate. Propelling charges have a subsonic burn rate. Propelling charges are more controllable and produce a propulsive force when they combust. (Kubota, 2007).

Since the 13th century until the first half of the 19th century, black powder was the only available propelling charge. In the second half of the 19th century, new types of propelling charges were introduced. They are known as smokeless propellant, gun propellant, or propellant. Gun propellant has several advantages over black powder. When black powder combusts, it produces substantial quantities of smoke and residues within the gun barrel. Modern gun propellant has a clean, smokeless combustion. Black powder is very hygroscopic, where it absorbs moisture, unlike gun propellant. Black powder is unstable where an electrostatic spark is sufficient to ignite it. Gun propellant, conversely, is more stable. Black powder is still in use today for a very limited number of applications, such as flame enforcers in igniters and within some pyrotechnical applications (Dyckmans, 2015).

Gun propellant is composed of powerful, metastable energetic materials that are capable of producing high-temperature gases that contain a vast amount of energy. They are smokeless, stable, powerful, and controllable. They come in the form of loose grains. These grains are usually contained in either metallic or combustible cases.

Gun propellant, as a term, is very generic. There are different types of gun propellants that differ based on their chemical composition. They are categorized as single-base propellant (SBP), double-base propellant (DBP), and triple-base propellant (TBP).

Single-base propellant consists primarily of nitrocellulose, which is nitrated cotton fibers (cellulose). Its ignition temperature is approximately 315 ºC. It has a flame temperature that ranges between the temperatures of 2230 °C and 2730 ºC. The flame temperature of SBP is relatively low and is consequently classified as a cool burning propellant. The energy content of SBP reaches up to 1050 joules per gram. It is the least energetic among the various propellant types (Kubota, 2007).

Double-base propellant is primarily composed of nitrocellulose and nitroglycerine, which is very sensitive powerful explosive. The presence of nitroglycerin in the composition elevates the energy content, the flame temperature, and reduces the ignition temperature. The ignition temperature of DBP is approximately 145 ºC. Its flame temperature ranges between 2330 °C and 3330 ºC. DBP has an energy content of approximately 1170 joules per gram. DBP is classified as the most sensitive and powerful of the various propellant types (Kubota, 2007).

Triple-base propellant contains an additional energetic component in conjunction with nitrocellulose and nitroglycerine, known as nitro-guanidine. Triple-base propellant has a moderately higher energy content at a relatively lower flame temperature. It has a typical energy content of approximately 1100 joules per gram and flame temperature that is less than 2430 ° C. It is consequently also classified as a cool burning propellant (Kubota, 2007).

Ballistic systems are driven by means of gas generated by propellant grains. Ballisticians can control the entire ballistic system to meet their predominant designated requirements by manipulating the rate of gas generated by propellant grains. The rate of gas generation can consequently be controlled by manipulating the exposed surface of the grain. As a result, the shape of the propellant grain is extremely important. It allows for the performance customization of the ballistic system. There are numerous different propellant grains that differ in geometries to deliver required gas production profiles. They are categorized as (Carlucci, 2007):

- digressive burning grains;
- neutral burning grains; and
- progressive burning grains.

A digressive burning grain, once it starts to burn, will experience a decrease in its total surface area over time. Figure 3 shows an illustration of a digressive burning grain (cylindrical grain). It is noticeable that the total surface area reduces over time, with a corresponding reduction in gas production (Carlucci, 2007). The maximum rate of gas generation in digressive grains is at the initial phase of burning.

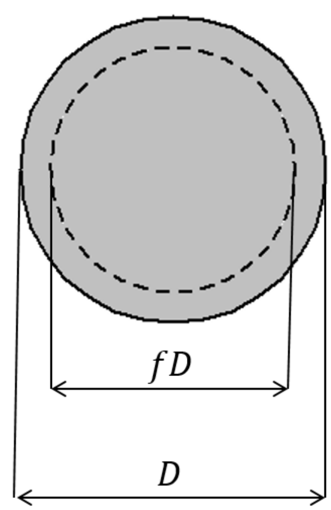

Figure 3: Cylindrical grain

In Figure (3) D is the thickness of propellant between any two surfaces and fD is the web remaining at any time.

A neutral burning grain's total surface area remains constant over time once it starts to burn. The benefit of this is found in gas generation, which remains constant over time. Figure 4 is an illustration of a neutral burning grain (perforated cylindrical grain). It is noticeable that as it burns, the perforation diameter enlarges and the outer diameter shrinks in simultaneous pattern, effectively compensating for each other. This mechanism keeps the total exposed surface of neutral grains unchanged (Carlucci, 2007). Consequently, the rate of gas generation in neutral grains is almost constant from the start to the end.

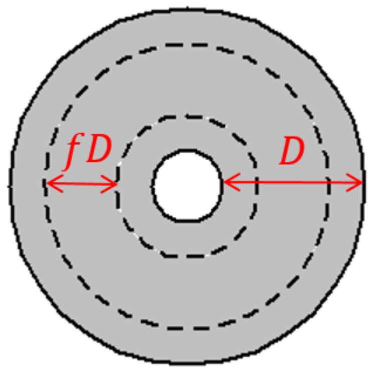

Figure 4: Single perforation grain

Progressive burning grains are characterized with a total surface area that increases over time as it burns. The rate of gas evolution consequently increases with burning time up to a certain point in time, after which it rapidly depletes. Figure 5 is an illustration of a progressive burning grain (multi-perforated cylindrical grain). It is noticeable that as it burns, the seven perforations enlarge, whilst the outer diameter simultaneously shrinks. This configuration results in the total surface area increasing over time (Carlucci, 2007). Progressive grains increase the chamber pressure slower than the other grains. The maximum rate of gas generation in progressive grains is experienced at the final phase of burning.

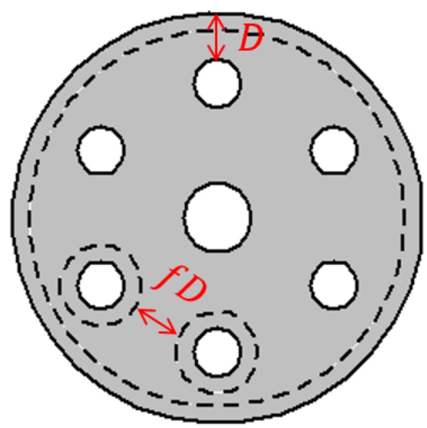

Figure 5: Seven perforations grain

Figure 6 shows the burning profiles of the cylindrical grain (digressive), single perforation grain (neutral), and seven perforations grain (progressive) with respect to their surface area. The vertical axis represents the fraction of the total surface area of propellant grain. The horizontal axis represents the fraction of volume regression. When the fraction of volume regression is equal to 0, it means that the propellant grain did not start to burn yet. However, when the fraction of volume regression is equal to 1, it means that the propellant grain is fully combusted.

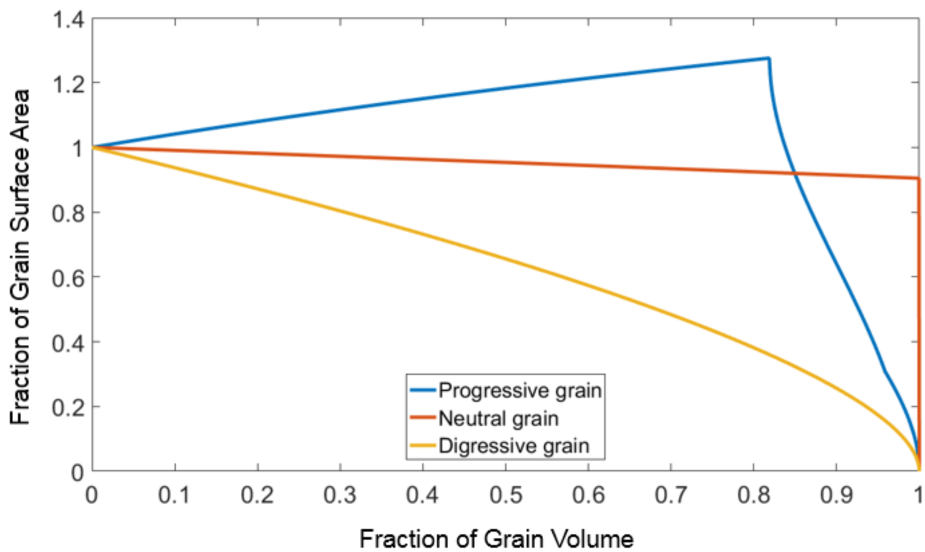

Figure 6: Grain surface area progression vs grain volume regression

As was mentioned, the gas production rate depends on the total exposed surface area of the grain. As can be seen in Figure 6, the maximum surface area of the digressive grain is at the initial burning, as illustrated in Figure 6. Consequently, the maximum rate of gas production is delivered at the initial phase of burning. After that, the gas production of digressive grains falls as the surface area decreases. As the progressive grain start to burn, however, its surface area starts to increase. The maximum surface area of the progressive grain is achieved when the fraction of volume regression is between 0.7 and 0.8, as illustrated in Figure 6. Consequently, the maximum rate of gas production is delivered at that moment. Conversely, a neutral grain's surface area is almost constant throughout burning, as illustrated in Figure 6. Consequently, the rate of gas production is almost constant.

1.1.1.3 Igniter

An igniter is a device that contains a small quantity of extremely sensitive explosives such as lead-azide, lead-styphnate, or tetrazene. These explosives within the ignitor are activated by either electric current or percussion. When activated, these explosives propagate hot gases and burning particles through gun propellants to ignite them. The igniter's main function is to simultaneously ignite all the grains of gun propellant. When the gun propellant mass is relatively small, explosives are sufficiently strong enough to properly ignite the entire propellant charge. However, when gun propellant mass is relatively large in conjunction to a complicated layout, the explosives on its own are not sufficiently strong enough to ignite the entire charge. In these conditions the igniter is coupled with a flame enforcer, such as black powder, to ensure proper ignition of the gun propellant charge (Dyckmans, 2015).

1.1.1.4 Projectile

The projectiles can only be stabilized during flight by means of induced spinning (spin-stabilized projectiles) or fins (fin-stabilized projectile).

Spin-stabilized projectiles are only compatible with rifled-bore barrels. They are fitted with a metallic band, which is known as a rotational band or driving band. Usually, the rotational band has a slightly larger diameter than the rifled-bore. When the projectile starts to move through the rifled-bore, the rotational band engraves into the circumferential grooves, which induces rotation on the projectile. Rotational bands have two functions. The primary function is to impart rotational motion onto the projectile to stabilize it after exiting the gun. The secondary function is to work as a seal between the projectile and the rifled-bore to prevent propellant gas from escaping between the projectile and the bore as pressure builds up. Figure 7 shows an illustration of a spin-stabilized projectile fitted with a rotational band.

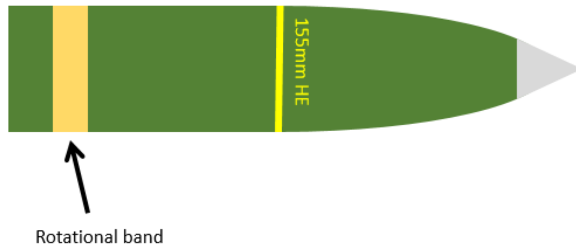

Figure 7: Spin-stabilized projectile

Fin-stabilized projectiles are only compatible with smooth-bore barrels. They are fitted with a tail and fin extension to stabilize the projectile during flight after exiting the gun. Fin-stabilized projectiles usually have the same diameter as the smooth-bore or slightly less. They are fitted with a polymer ring that expands under pressure. The polymer ring also functions as a seal between the projectile and the smooth-bore to avoid the high-pressure gas from leaking between the bore and the projectile. Figure 8 shows an illustration of fin-stabilized projectile.

Figure 8: Fin-stabilized projectile

1.1.2 Ballistic systems classifications

There are countless numbers of different ballistic systems in use around the world. Each ballistic system differs in its design and its performance level. Ballistic systems are classified based on their bore diameter, also known as their caliber. The main ballistic systems classifications are small caliber systems, medium caliber systems, and large caliber systems.

Small caliber systems have a caliber less than 20 millimeters (mm) in diameter. The majority of small caliber systems are handheld, and they are used to engage with targets ranging between tens to several hundreds of meters. These systems are capable of firing projectiles with a wide range of velocities ranging from 300 meters per second (in the case of a handheld gun) to 1000 meters per second (in the case of rifles). The kinetic energy of small caliber projectiles can reach up to 4000 joules. The majority of small caliber systems have an interior ballistic cycle that lasts for only one millisecond (Dyckmans, 2015).

Medium caliber systems normally have a caliber that ranges between 20 mm to 76 mm. Most medium caliber systems are installed on armored vehicles and they are used to engage with targets that are a few hundred to a few thousand meters away. Most medium caliber systems fire their projectiles at supersonic velocities. Some medium caliber systems fire their projectiles to the designated targets indirectly such as the mortar system. They fire kinetic energy projectiles and explosive energy projectiles (Dyckmans, 2015).

Large caliber systems are known as artilleries and have a caliber that exceeds 76 mm. Artilleries predominantly fire projectiles along curved trajectories. As a result, they can engage with targets over very long distances that can reach up to 70 kilometers. Large caliber systems operate at muzzle velocities that can reach up to a 1000 meters per second. The majority of large caliber systems fire explosive energy projectiles (Dyckmans, 2015). The best example that represents large caliber systems is a 155 mm artillery system.

A 155 mm artillery system is designed to provide ground support for infantries and armored forces at vast distances, which could reach up to 70 kilometers. The 155 mm artillery system is available in the form of the self-propelled system such as G6 or towed howitzers. A 155 mm artillery system consists of a rifled-barrel. The length of the barrel can reach up to eight meters long. A 155 mm artillery system fires spin-stabilized projectiles at supersonic speed. The propellant charge mass of a 155 mm artillery system can weigh up to 16 kilograms (GICHD, 2018). This research will only focus on the 155 mm artillery system and other ballistic systems will not be included in the scope of this research.

1.1.3 Interior ballistic cycle of a generic ballistic system

The interior ballistic cycle can be described through all the phenomena relating to propellant ignition, projectile motion, as well as gun motion from ignition until the projectile leaves the muzzle. Although the interior ballistic cycle seems identical for all gun systems, it differs in its details from one ballistic system to another.

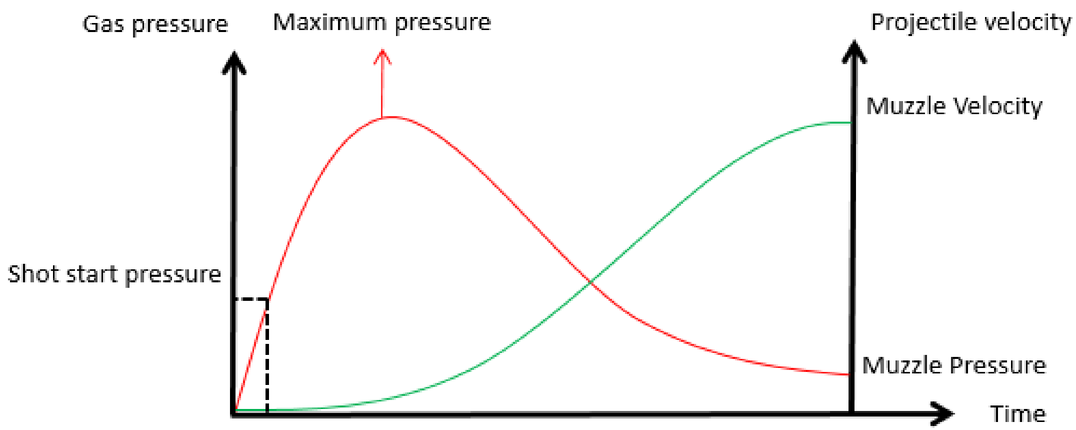

Figure 9: Gun chamber pressure and projectile velocity vs projectile displacement

An interior ballistic cycle of a generic ballistic system is explained briefly in logical sequential steps as follows:

1. The interior ballistic cycle commences when the igniter device explodes.
2. Hot gases and burning particles are propagated through the solid propellant grains.
3. Solid propellant grains are ignited and start to burn.
4. As propellant grains burn, they liberate hot gas that contain vast quantities of energy.
5. Pressure and temperature inside gun chamber start to increase, see Figure 9.
6. Pressure increases inside gun chamber forces solid propellant grains to burn at an accelerated rate, causing rapid increase in chamber pressure, see Figure 9.
7. High gas pressure inside the gun chamber exerts force on the projectile base, the chamber sidewalls, and the breechblock.
8. When the pressure on the projectile’s base becomes high enough, the projectile is propelled through the gun barrel, see Figure 9.
9. The projectile starts to accelerate within the barrel, increasing the volume of the gun chamber.
10. Pressure inside the gun chamber start to decrease as the projectile continues to increase speed due to gas mass flow produced by the burning solid propellant grains, see Figure 9.

11. At a certain point, solid propellant grains are completely burnt out, but the expanding gas mass is still sufficient to propel the projectile even further, see Figure 9.
12. The projectile leaves the gun muzzle with a high velocity.
13. The projectile is followed by a blast discharge from the barrel, which is caused by a significant pressure wave.

The time duration of an interior ballistic cycle only lasts for a few milliseconds for small- and medium caliber systems. In large caliber systems, the timespan barely reaches 15 milliseconds. Figure 9 illustrates pressure profile, as well as projectile velocity profile inside the ballistic system during the interior ballistic cycle.

1.1.4 Interior ballistic cycle simulations

The field of interior ballistics has been around for centuries. Various research studies and projects have contributed to a better understanding of the physics involved with internal ballistics, as well as the mathematical description of internal ballistics. Some of the world's greatest physicists and mathematicians, such as Lagrange and Isaac Newton, contributed directly or indirectly to solve interior ballistics related problems. Today, there are empirical, analytical, and numerical models available that describe the interior ballistic cycle. The majority of interior ballistic simulations are executed by means of numerical models. Interior ballistic numerical models can be categorized as:

1. Lumped Parameter Model (LPM) for interior ballistics. Also, known as (IB0D);
2. Interior Ballistic 1-Dimentional model (IB1D); and
3. Interior Ballistic 2-Dimentional model (IB2D).

Each model is used for a specific application. The Lumped Parameter Model (LPM) consists of several sub-models and it is used to predict the projectile's exit velocity or muzzle velocity, and the maximum chamber pressure of a ballistic system. The IB1D model is used to simulate the axial pressure waves, gas flow constraints, multi-stage ignition of non-uniform propellant charges. The IB2D model is used to simulate complex ignition trains, radial charge layouts, high-low pressure systems, and perforated primers (Consultancy, 2018). This research, however, will only focus on the LPM and other numerical models of interior ballistics will not be included in the scope of this research.

1.1.5 Lumped Parameter Model of Interior Ballistic

The LPM is internationally accepted as an efficient and practical solution to perform fast and accurate interior ballistic calculations (Dyckmans, 2015). Even though it seems not as sophisticated as the IB1D or the IB2D models, it still plays a vital role in ballistic system development.

The LPM is practical and convenient. According to Schabort (2016) up to 80 percent of IB cycle simulations during work routines are conducted using IB0D models, and a wide range of beneficial data can be derived from it. These models are extremely robust.

The LPM is important during the development of a ballistic system from the conceptual phase to the optimization phase. It can determine whether or not it is safe to fire such a weapon with a particular mass of propellant. In addition, it can solve the entire pressure curve of a ballistic system. A ballistic system manufacturer can consequently determine the dimensions of the gun. It is also widely used for propellant charge optimization (Dyckmans, 2015). Therefore, improvement on the accuracy of IB0D models delivers numerous advantages during gun system designing phases, which would assist ballisticians to optimize gun system design, minimize costs, and control changes.

The LPM of interior ballistics consists of several models that are lumped together to simulate the interior ballistic cycle of a ballistic system. These models are the combustion model, energy model, equation of state, pressure gradient model, and the equation of motion, respectively. The combustion model solves the propellant grain's combustion. The energy model calculates the available energy in propellant gas through the principle of conservation of energy, which states that, the amount of energy remains constant. Energy is neither created nor destroyed, but transforms from one form to another. The equation of state solves the space-mean pressure inside the gun chamber during the ballistic cycle. The pressure gradient model solves for the pressure exerted at the breech, as well as the projectile's base. Lastly, the equation of motion solves the motion of the projectile and the gun. Each of the above-mentioned models shall be described in more detail in Chapter 2.

The North Atlantic Treaty Organization (NATO) has standardized a LPM that is known as STANAG or STANAG 4367. The LPM of STANAG 4367 is to be used for interior ballistics simulation. It is widely accepted among ballisticians as the most accurate LPM for interior ballistic simulation.

1.2 Problem statement

During work routines, it is noticed that when the LPM of STANAG 4367 is used to simulate a 155 mm artillery system, it predicts the muzzle velocity and maximum chamber pressure with relatively large deviations from the measured values. The deviation between the predicted and the measured values is approximately four percent. From a ballistician's prospective, four percent is relatively large. Therefore, the model needs major calibration to match the measured values, which leads to confidence loss between the ballistician and her/his model.

There is a sub-model of the energy model that calculates the heat transfer from the propellant gas to the gun wall. It is known as the heat transfer model. It was found to be that the heat transfer model of STANAG 4367 is not suitable for simulating a 155 mm artillery system. According to Dyckmans (2015) the heat transfer model plays a significant role in the accuracy of the LPM of interior ballistics (Dyckmans, 2015). The problem with the heat transfer model of STANAG 4367 is that it utilizes a nominal thickness of the gun wall in order to calculate the heat transfer. However, it is difficult to determine a nominal wall thickness for a 155 mm artillery system because it significantly varies from the breech to the muzzle. According to Schabort (2016) it is challenging to guess a nominal wall thickness for such a system. Furthermore, it is clear that if the nominal wall thickness is underestimated or overestimated, the heat transfer calculations will not be accurate. Therefore, the predictions of the LPM of STANAG 4367 would be affected accordingly.

1.3 Explicit formulation of the research

The primary aim of this research is to find a better alternative to the heat transfer model of STANAG 4367 that is more suitable for a 155 mm artillery system. This research also aims to develop a practical interior ballistic simulation program to be used in different applications of interior ballistics. It also aims to provide guidelines for interior ballistic simulation procedures when the ballistic system has a constant or variable gun wall thickness.

1.4 Methods of investigation

The methods of investigation are as follows:

1. A literature study that describes the LPM of STANAG 4367 shall be conducted. In addition, the literature study will highlight several variations of heat transfer models that can be used as alternatives to the heat transfer model of STANAG 4367.

2. An interior ballistic simulation program, which will be STANAG 4367 compliant, shall be developed using MATLAB. This simulation program will be the fundamental tool to serve the primary aim of the research, which is to suggest a better alternative to the heat transfer model of STANAG 4367. The interior ballistic simulation program will be verified against the interior ballistic simulation program of Rheinmetall Denel Munition (Pty) Ltd (RDM). The interior ballistic simulation program of RDM is STANAG 4367 compliant and it has been in RDM's service for almost 20 years. Throughout these years, the interior ballistic simulation program of RDM has been regularly improved. It is extensively utilized in product development and is verified and validated. It has been tested against hundreds of ballistic systems from small caliber to large caliber systems.

3. The variations of the heat transfer model, which are discussed in the literature review, will be lumped into the developed interior ballistic simulation program. Each heat transfer model variation will be verified by making sure there is no oscillation or discontinuity in the result obtained via the variation itself.

4. The 155 mm artillery system shall be simulated using all the discussed variations of heat transfer model, one at a time. Then, the simulations outputs shall be analyzed and compared against actual measured muzzle velocity and maximum chamber pressure of a 155 mm artillery system.

5. The most suitable variation of the heat transfer model for a 155 mm artillery system, which results in positive improvement, shall be highlighted and recommended.

6. The developed LPM that has the suitable variation of heat transfer model shall be validated against different configurations of a 155 mm artillery system.

1.5 Research objectives and contributions

The objectives and contributions of this research are as follows:

1. Suggest a better alternative heat transfer model than the heat transfer model of STANAG 4367.

2. Provide guidelines for interior ballistic simulation procedures when the ballistic system has either a constant or a variable gun wall thickness.
3. Provide a practical interior ballistic simulation program to be used in different applications of interior ballistics.

1.6 Scope of research and study limitation

1. The study shall only be conducted on a 155 mm artillery system.
2. The measured data, which are needed for this research, is limited.
3. The number of 155 mm artillery system configurations are limited.

1.7 Dissertation outline

Chapter 2: Literature review:

In Chapter 2, the essential literature related to the research focus is provided. The LPM of STANAG 4367 shall be described in more detail. An alternative heat transfer model shall be proposed for the investigation.

Chapter 3: Methodology:

In Chapter 3, an interior ballistic simulation program shall be developed to serve the main purpose of the study. Furthermore, the interior ballistic simulation program shall be verified against the interior ballistic simulation program of RDM. The proposed heat transfer models shall be included in the interior ballistic simulation program to perform the investigation, which is to select the most suitable heat transfer model for simulating a 155 mm artillery system.

Chapter 4: Modelling:

In Chapter 4, the 155 mm artillery system that is included in the investigation shall be briefly described. The measured muzzle velocity and maximum pressure of the system shall be obtained. The 155 mm artillery system shall be simulated using all different heat transfer models. The most suitable heat transfer model shall be recommended. The recommended heat transfer model shall be used in the LPM and validated against different configuration of the 155 mm artillery system.

Chapter 5: Conclusions and recommendations:

In Chapter 5, an overview of the research and the final conclusion shall be drawn. The recommendations shall be made. Furthermore, further study for future research shall be made.

1.8 Summary

In this chapter, the essential background prior to the problem statement of the research was provided. The problem statement as well as the explicit formulation of the research were provided. The methods of investigation of the research were outlined. The research objectives and contribution and study limitations were described. The following chapter focuses on providing the literature that supports the main purpose of the research.

Chapter II Background Study

2.1 Introduction

In this chapter, the interior ballistic cycle will be described in further detail. The sub-models of the LPM of STANAG 4367, which are the combustion model, energy model, equation of state, pressure gradient model, and equation of motion are going to be described. The utilized assumptions of the LPM will be listed. Also, several variations of the heat transfer model are going to be formulated.

2.2 Interior ballistic cycle

Figure 10 illustrates the internal layout of loaded ballistic system.

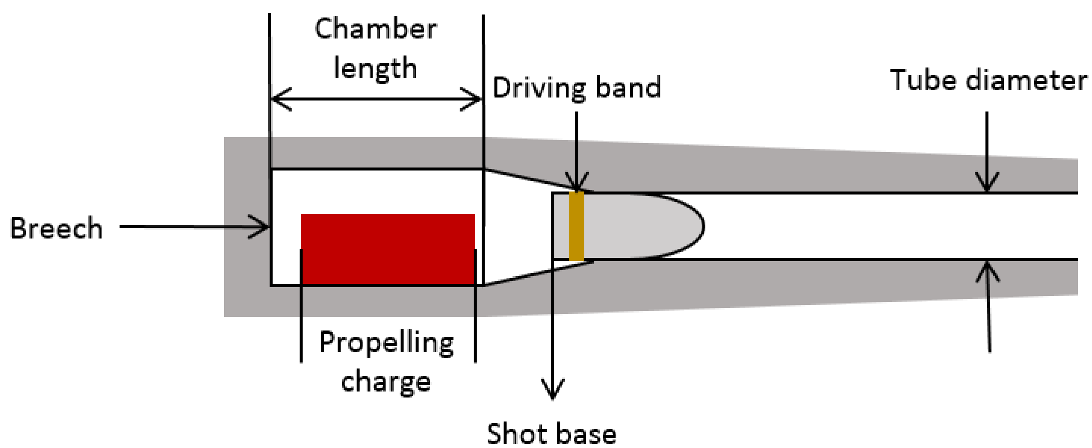

Figure 10: Internal layout of loaded gun system

The interior ballistic cycle typically starts when a striker impacts the igniter. The igniter explodes, propagating hot gases and burning particles through the entire propellant grains. Propellant grains are initiated and start to burn almost simultaneously. Propellants start to liberate hot gases, thus pressure starts to build up inside gun chamber. The projectile is still stationary at this stage since the pressure on projectile's base is less than the shot start pressure. The shot start pressure is the pressure required to move the projectile from its initial loaded position.

As the chamber pressure continues to increase, the propellant grains burn more intensely, causing chamber pressure to rapidly increase. When the chamber pressure matches the shot start pressure, the projectile starts to move. The engraving of the rotational band into the circumferential grooves commences at this point.

The pressure inside the gun chamber is significant at this stage. After the rotational band is entirely contained within the grooves, the frictional force between the rotational band and bore wall significantly decreases. Thus, the projectile starts accelerating. Due to the circumferential grooves, the projectile also picks up a rotational motion. As the projectile moves through the barrel, the chamber volume starts to increase, causing the pressure to decrease. However, propellant grains are still liberating enough gas to compensate for the extra volume created by the projectile's forward motion. At a certain point, the volume becomes relatively large so that the gas mass liberation from propellant grains cannot compensate any further. As a result, the pressure inside the gun chamber starts to decrease. However, the projectile is still accelerating due to the relatively large mass flow of the propellants gases.

At a certain point in the cycle, known as all burnt, all the propellant grains are completely combusted. As the projectile moves toward the muzzle, pressure inside the chamber decreases. The projectile exits the muzzle with a muzzle velocity that reaches hundreds of meters per second. The exiting projectile is followed by a blast due to high-pressure gas exiting the muzzle. Figure 11 illustrates the chamber pressure curve inside gun system against the projectile translation.

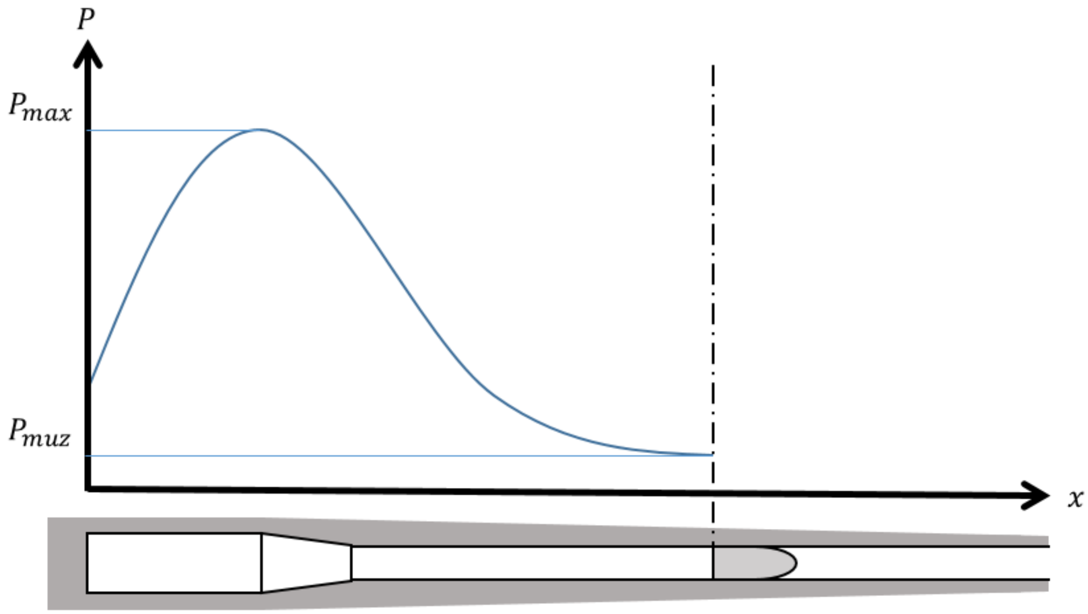

Figure 11: Chamber pressure profile with respect to gun system

As can be seen in Figure 11, the peak of the curve represents the point where the maximum pressure occurs with respect to projectile displacement. As the projectile starts to move, the volume behind the projectile starts to increase. Thus, the chamber pressure starts decreasing.

2.3 The Lumped Parameter Model of STANAG 4367

The LPM of STANAG 4367 is widely accepted among ballisticians as the most up-to-date model to perform efficient and accurate interior ballistic calculations (Schabort, 2016). When the LPM simulates a ballistic system, it solves the entire interior ballistic cycle and generates valuable predictions especially for the ballistic system manufacturers, propellant manufacturers, ballisticians, and users of ballistic systems (Dyckmans, 2015). These predictions are:

1. Maximum chamber pressure.
2. Maximum acceleration of the projectile.
3. Muzzle velocity of the projectile.
4. Maximum spin rate of the projectile.
5. Maximum projectile's base pressure.
6. Maximum gas generated rate from propellants.
7. Barrel exit pressure.

8. Barrel exit time.
9. Time at the maximum pressure.
10. All burnt time of the propellants.
11. The time duration of the interior ballistic cycle.
12. The maximum wall temperature of the bore.
13. Ballistic system efficiency.
14. Maximum projectile kinetic energy.
15. Gun backward velocity due to recoil.

As was mentioned in Chapter 1, the LPM of interior ballistics consists of several models that are lumped together to solve the interior ballistic cycle of a ballistic system. These models are the combustion model, energy model, equation of state, and equation of motion. Figure 12 shows a flowchart of the structure of the LPM of interior ballistics.

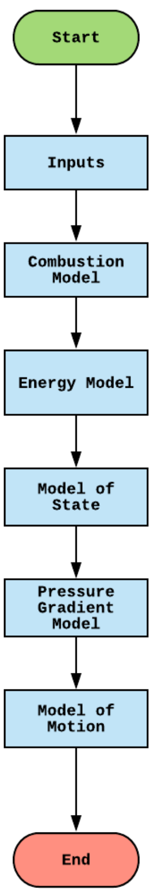

Figure 12: Flowchart of LPM of interior ballistics

The combustion model assumes the propellant charge is ignited and solves the propellant charge combustion. The combustion model generates the propellant gas and solid masses to the energy model. The energy model calculates the available energy in propellant gas and generates it to the equation of state. The equation of state calculates the space-mean pressure in the gun chamber and generates it to the pressure gradient model. The pressure gradient model solves the amount of pressure exerted on the base of the projectile and the breech of the gun and generates them to the equation of motion. The equation of motion solves acceleration, velocity, and displacement of the projectile and gun. Each of the above-mentioned models are described according to STANAG 4367 in more detail in the sections that follow.

2.3.1 Combustion model

The combustion model calculates the amount of gas generated by propellant grains when ignited. The combustion model consists of several equations, which are burning rate equation, form function equations, the fraction of propellant mass burning rate equation, and the fraction of propellant mass burned equation. Propellant grains burn at a certain rate and this burn rate depends on two main factors:

1. The chemical composition of the propellant plays a vital role in the propellant's burn rate. If the grain contains high-energetic materials such as nitroglycerine, it burns faster and vice versa.

2. The burning rate of propellant grain is significantly impacted by its surrounding pressure. Russel (2009) explains that, "it is universally accepted that the higher the pressure, the greater the heat transfer onto the surface of the grain and hence, the higher the rate of burning". A propellant's burn rate is directly proportional to the surrounding pressure. When the surrounding pressure is relatively high, propellant the grain burns faster. However, when the surrounding pressure is relatively low, the grain burns relatively slower.

Equation (1), known as Vieille's law, mathematically describes propellant burning rate (r). This equation was introduced by a French chemist in 1893 with the name of Paul Vieille. In the case of a ballistic system, the constants (β) and (α) are dependent on the grain's chemical composition, whilst ($\overline{P}$) represents the space-mean pressure of the gun chamber (Moreno, 2009).

$$r = \beta(\bar{P})^{\alpha}, \quad (1)$$

However, *how* the propellant grain burns, remains questioned. Piobert's law states that, "burning of propellant grains takes place by parallel layers where the surface of the grain regresses, layer by layer, normal to the surface at every point" (Russell, 2009). This means that propellant grains exhibit linear burning behavior. As propellants regressively burn, it burns from all directions and retains its geometrical shape until dissipation. Even if the propellant grain is less than one millimeter in diameter, Piobert's law is still applicable (Russell, 2009). Consequently, when a spherical propellant grain starts to burn regressively, it burns layer by layer from all directions whilst maintaining its spherical shape until it completely dissipates. Figure 13 is an illustration of how a spherical grain maintains its geometrical shape throughout burning. It can be seen that the total surface area of the grain is shrinking while its geometrical shape is retained.

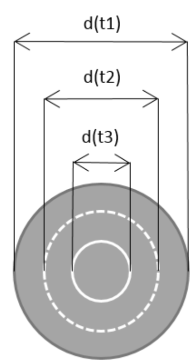

Figure 13: Burn progress (sphere)

Where

$d(t)$ The grain's diameter during burning at certain time,

As propellants regressively burns, it generates gas at a certain rate. The rate of gas liberation is dependent on the total exposed surface of propellant grains. The combustion model has to know the initial exposed surface area and volume of the propellant grain in order to calculate the exact amount of gas generated. As a result, the combustion model is coupled with a form function equation. Form function equations are analytical equations that calculate the propellant grain's surface area and volume. Equation (2) and Equation (3) are the form function of a spherical grain (Moreno, 2009):

$$V = \frac{1}{6}\,\pi(D)^3, \quad (2)$$

$$S = \pi(D)^2, \quad (3)$$

Where:

V Propellant grain volume,

D Propellant grain diameter,

S Propellant grain surface area,

The complexity of the form function equation depends on the propellant grain geometry. The above mentioned form function equation is the simplest because it describes a sphere. However, the form function equation of the seven perforations grain, for instance, would be much complicated.

After the burn rate is calculated, the burn rate is integrated to determine the burned distance. The surface area and volume of the propellant grain can be updated by the form function. After that, the mass fraction burning rate of the propellant grain is calculated. Equation (4) represents the mass fraction burning rate (Moreno, 2009):

$$\frac{dZ}{dt} = \frac{S * r}{V_g}, \quad (4)$$

Where:

Z Mass fraction burning rate of the propellant grain,

S Propellant grain surface area,

V_g Initial volume of the propellant grain,

By integrating the mass fraction burning rate of the propellant grain, the mass burned fraction can be calculated. Equation (5) represents the mass burned fraction:

$$Z = \int_0^t \dot{Z}\, dt\ , \qquad (5)$$

Where:

Z The fraction of mass burned of the propellant,

The exact amount of gas generated from the propellant grain can be calculated using the mass burned fraction. The combustion model centers around the principle of conservation of mass, which states that, the amount of mass remains constant; mass is neither created nor destroyed. In other words, the decrease of the propellant solid mass is consequently equal to the increase of the propellant gas mass. It is possible now to determine the gas mass generated by the propellant grains and the solid mass remained at any given moment using the fraction of mass burned, see the following:

$$C_{solid} = (1 - Z) * C\ , \qquad (6)$$

$$C_{gas} = Z * C\ , \qquad (7)$$

Where:

C_{solid} Mass of solid propellant grains,

C_{gas} Mass of propellant gas,

C Initial total mass of propellant,

The flowchart in Figure 14 summarizes the structure of the combustion model.

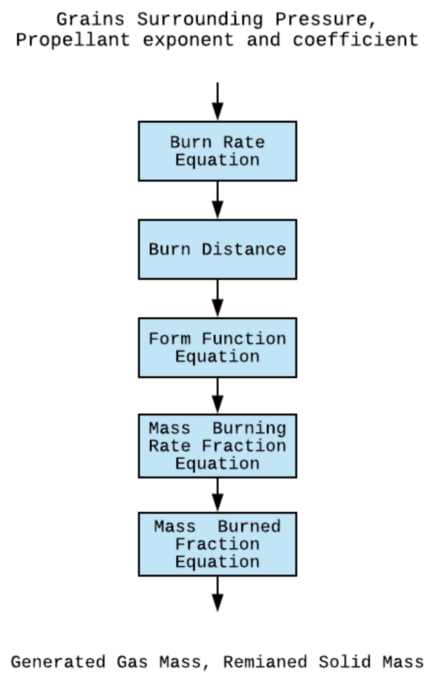

Figure 14: Combustion model flowchart

The inputs required by the combustion model are the space-mean pressure, propellant grain exponent and coefficient, respectively. The inputs are processed by the burn rate equation to generate the current burn rate and burned distance. After that, the surface area and volume of the grain are updated via form function equations. Then, the mass burning rate fraction and the mass burned fraction are calculated. Finally, gas mass generated and solid mass remained are generated to the energy model.

2.3.2 Energy model

The energy model forms the core of the LPM of interior ballistics. The principle of the energy model centers around the principle of conservation of energy. The conservation of energy states that, the amount of energy remains constant. Energy is neither created nor destroyed, but transforms from one form to another.

During the exothermic reaction of propellant grains, hot gases that are capable of performing work are released. The work energy or force constant of the propellant gases can reach up to 1200 J/g. The work energy transforms into useful and non-useful (loss) energies. From an interior ballistics prospective, any energy that does not contribute in projectile acceleration is considered as a loss. The correct estimation of these energies remains one of the major difficulties that ballisticians face (Dyckmans, 2015). Equation (8) calculates the energy available in propellant gases is at any moment (Moreno, 2009):

$$T = \frac{\sum_{i=1}^{n} \frac{F_i' \, C_i Z_i}{\gamma_i - 1} + \frac{F_I C_I}{\gamma_I - 1} - E_{pt} - E_{pr} - E_p - E_{br} - E_r - E_d - E_h}{\sum_{i=1}^{n} \frac{F_i' \, C_i Z_i}{(\gamma_i - 1) T_{0_i}} + \frac{F_I C_I}{(\gamma_I - 1) \, T_{0_I}}}, \quad (8)$$

Where:

n Number of propellants,

F_i' Adjusted force per unit mass of i^{th} propellant,

F_I Force per unit mass of igniter propellant,

C_I Initial mass of igniter,

γ_i Ratio of specific heats for i^{th} propellant,

γ_I Ratio of specific heats for igniter,

E_{pt} Energy consumed due to projectile translation,

E_{pr} Energy loss due to projectile rotation,

E_p Energy loss due to propellant gas and unburned propellant motion,

E_{br} Energy loss due to friction and engraving of rotating band,

E_r Energy loss due to recoil,

E_d Energy loss due to air resistance,

E_h Energy loss due to heat transfer to the chamber and barrel walls,

T_{0_i} Adiabatic flame temperature of i^{th} propellant,

T_{0_I} Adiabatic flame temperature of the igniter,

Each of the above-listed energy losses are described according to STANAG 4367 in more detail in the points that follow.

1. Energy consumed due to the projectile translation (E_{pt}):

   Because propellant gas moves, it exerts a force on the projectile's base, causing it to accelerate. This acceleration requires energy. This energy is obtained from the total gas energy. In a 155 mm artillery system, the translation kinetic energy is approximately 28.3 percent of the total energy provided by propellant charge (Dyckmans, 2015). The projectile translation kinetic energy can be calculated as (Moreno, 2009):

$$E_{pt} = \frac{m_p v_p^2}{2}, \tag{9}$$

Where:

m_p Mass of the projectile,

v_p Velocity of the projectile,

2. Energy loss due to projectile rotation (E_{pr}):

   If the bore is rifled, the projectile not only receives translational kinetic energy, but it also receives rotational kinetic energy. However, the rotational kinetic energy is extremely small. In a 155 mm artillery system, projectile rotational energy consumes 0.4 percent of the total energy (Dyckmans, 2015). Equation (10) calculates the projectile rotational energy (Moreno, 2009):

$$E_{pr} = \frac{\pi^2 m_p v_p^2}{4T_W^2}, \tag{10}$$

Where:

T_W Twist of rifling,

3. Energy loss due to propellant gas and unburned propellant motion (E_p):

   During combustion, propellant gas and unburned grains are moving. Without this movement there would not be any pressure excreted on the projectile's base during the interior ballistic cycle. This motion of propellant gas and unburned grains consumes energy. The energy loss depends on the ballistic ratio, which is the propellant's charge mass to projectile mass ratio. As the ballistic ratio gets larger, the energy loss increases and vice versa. In a 155 mm artillery system, the motion of the gas and unburned propellant consumes in the order of 2.3 percent of the total energy produced by the propellant charge (Dyckmans, 2015). The energy loss due to propellant gas and unburned propellant motion can be calculated as (Moreno, 2009):

$$E_p = \frac{C_T v_p^2}{6}, \quad (11)$$

Where:

C_T Total mass of propellants and igniter,

4. Energy loss due to friction and engraving of rotating band (E_{br}):
If the bore is rifled, the engraving and friction between the projectile and the bore is very severe. The severity of this friction depends on the materials and dimensions of the barrel and the driving band. The projectile consequently requires energy to overcome the friction within the barrel. According to Dyckmans (2015) the projectile's engraving and friction in a 155 mm artillery system consumes up to 1.4 percent of the propellant's energy (Dyckmans, 2015). The energy loss due to friction and engraving of rotating band can be calculated as (Moreno, 2009):

$$E_{br} = A \int_0^x P'_R \, dx \, , \quad (12)$$

Where:

A Area of base of projectile including appropriate portion of rotating band,

P'_R Adjusted resistive pressure of the bore due to friction and engraving,

The profile of the resistive pressure of the bore due to friction and engraving, as proposed by STANAG 4367, is represented in Figure 15.

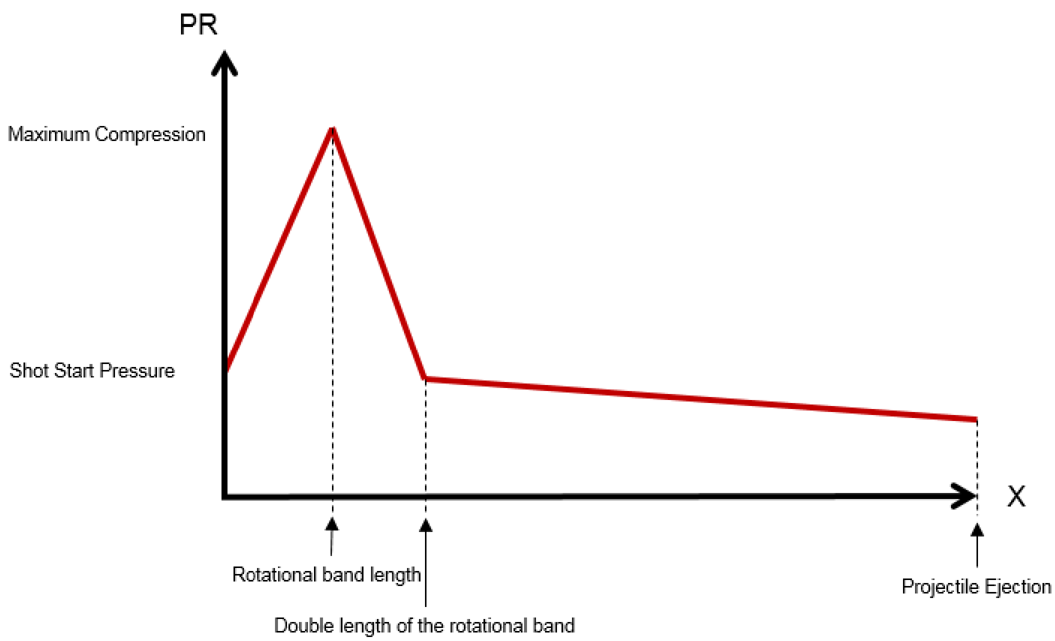

Figure 15: Resistive pressure profile due to driving band engraving and friction

The profile of resistive pressure is monitored by four points. These points are determined by empirical evidence. The resistive curve starts with the shot start pressure. As the driving band starts to fill the forcing cone, the resistive pressure starts to increase. After the driving band fills up the forcing cone, the driving band starts to penetrate into the grooves of the rifling and the resistive pressure increases. The resistive pressure reaches its peak (point of maximum compression) at the moment where the driving band is contained within the grooves. As the projectile starts to move, the resistive pressure starts to drop toward the third point. The third point is when the projectile moves at an equivalent distance of the length of the driving band. After that, the resistive pressure stays almost constant until the projectile and the driving band is ejected from the muzzle.

5. Energy loss due to recoil (E_r):
   High gas pressure exerts significant force on the gun's breech, causing the gun to accelerate in the opposite direction of the projectile during the internal ballistic cycle. The energy loss due to the recoiling of a 155 mm artillery is in the order of 1.3 percent of the total energy (Dyckmans, 2015). The energy loss due to recoil is expressed as (Moreno, 2009):

$$E_r = \frac{m_{rp} v_{rp}^2}{2}, \tag{13}$$

Where:

m_{rp} Mass of the recoiling parts,

v_{rp} Velocity of recoiling parts,

6. Energy loss due to air resistance (E_d):

   Air in front of the projectile (inside the barrel) is compressed as the projectile accelerates through the barrel. This causes a resistive pressure acting on the projectile's front surface. The pressure of the compressed air ahead of projectile depends on the projectile's acceleration. It can reach up to twenty times the ambient pressure. In a 155 mm artillery system, the energy loss due to air in front of the projectile is in the order of 0.1 percent of the total energy (Dyckmans, 2015). Equation (14) represents energy loss due to air resistance (Gronheim, 2000):

$$E_d = A \int_0^t v_p P_g \, dt, \tag{14}$$

Where:

P_g Pressure of gas or air ahead of projectile,

The pressure of gas or air ahead of projectile can be calculated as (Gronheim, 2000):

$$P_g = P_a \left[1 + \alpha_a M^2 \left(\frac{1 + \alpha_a}{4} + \sqrt{\left(\frac{1 + \alpha_a}{4} \right)^2 + M^{-2}} \right) \right], \tag{15}$$

Where:

P_a Pressure in the ambient air,

α_a Ratio of specific heats for air,

M Mach number of the projectile with respect to the air,

7. Energy loss due to heat transfer to the chamber and barrel walls (E_h):

Heat means energy. During propellant charge exothermic combustion, a large portion of its energy is transferred to the barrel walls (colder surroundings) by means of radiation and forced convection. The energy loss due to heat transfer is classified as the highest loss. In a 155 mm artillery, 2.6 percent of propellant charge energy is lost due to heat transfer (Dyckmans, 2015). The energy loss due to heat transfer to the chamber walls is calculated as (Moreno, 2009):

$$E_h = \int_0^t A_w h(T - T_c)\, dt\,, \tag{16}$$

Where:

A_w	Chamber wall area plus the area of gun tube wall exposed to the propellant gases,
h	Heat transfer coefficient of Nordheim, Soodak, and Nordheim,
T_c	Temperature of the chamber wall,

Because the projectile is moving during the interior ballistic cycle, the chamber volume behind the projectile enlarges. Thus, the wall exposed to propellant gases also enlarges. As a result, the chamber wall area plus the area of gun tube wall exposed to the propellant gases is calculated as (Moreno, 2009):

$$A_w = \frac{V_0}{A}\pi D_b + 2A + \pi D_b(x)\,, \tag{17}$$

The heat transfer coefficient of Nordheim, Soodak, and Nordheim is calculated as (Moreno, 2009):

$$h = \lambda \overline{C_p}\bar{\rho}\bar{v} + h_0\;, \tag{18}$$

Where:

λ	Nordheim friction factor,
$\overline{C_p}$	Specific heat at constant pressure of propellant gas,
$\bar{\rho}$	Mean gas density,

$\bar{v}$ Mean gas velocity,

h_0 Free convective heat transfer coefficient for air in the gun tube,

The Nordheim friction factor can be calculated as (Moreno, 2009):

$$\lambda = [13.2 + 4\log(100D_b)]^{-2} \ , \tag{19}$$

The temperature of the chamber wall can be calculated as (Moreno, 2009):

$$T_c = \frac{E_h + fE_{br}}{C_{pw}\rho_w A_w D_w} + T_{0_w} \ , \tag{20}$$

Where:

C_{pw} Heat capacity of steel of chamber wall,

ρ_w Density of chamber wall steel,

A_w Chamber wall area plus area of gun tube wall exposed to propellant gases,

D_w Chamber wall thickness heated,

T_{0_w} Initial temperature of chamber wall,

As can be seen, to calculate the temperature of the chamber wall, the equation requires a nominal value of the chamber wall thickness. In a 155 mm artillery system, however, the chamber wall is not uniform. In addition, it is challenging to determine a nominal chamber wall thickness for such a system. The equation of chamber wall temperature plays a significant role in calculating the energy loss due to heat transfer. Because the energy loss due to heat transfer weighs the most, it affects the accuracy of the LPM of STANAG 4367. As a result, if the nominal chamber wall thickness is underestimated or overestimated, the predictions of the LPM of STANAG 4367 would be impacted.

Figure 16 shows a chart that compares all the above-mentioned energy losses.

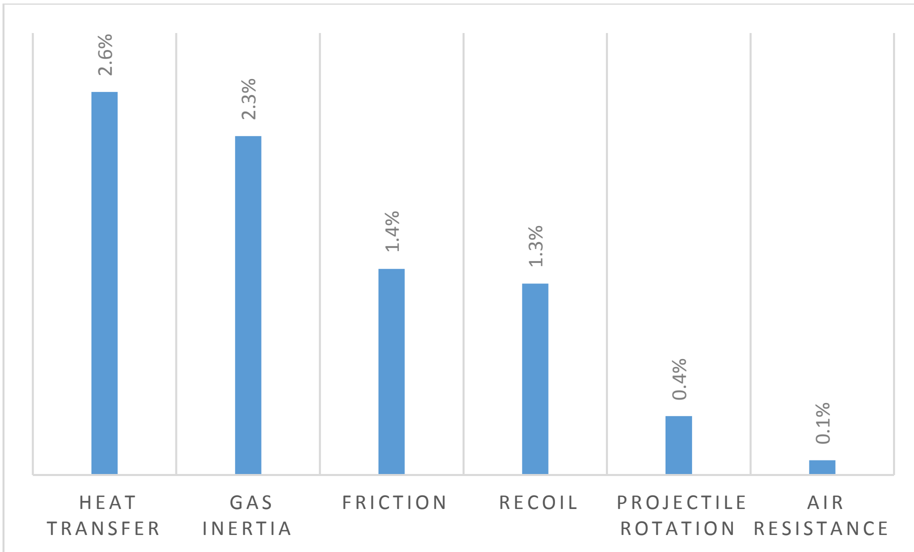

Figure 16: Energy losses comparison of 155 mm artillery

As can be seen, the losses are rearranged from the largest loss to the smallest. The heat transfer energy loss weighs the most. Conversely, the energy loss due to air resistance weighs the least. Figure 17 shows the flowchart of the energy model.

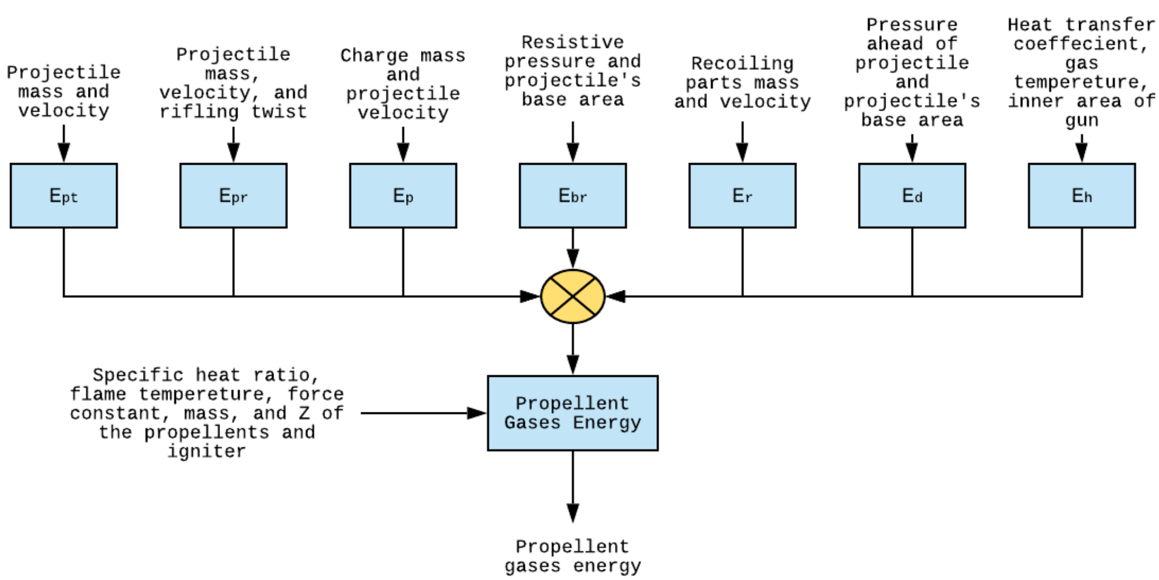

Figure 17: Energy model flowchart

After all the energy losses are calculated, the available energy in gas propellants can be calculated and generated to the equation of state.

2.3.3 Equation of state

When propellant's gas energy is determined, the equation of state is able to compute the space-mean chamber pressure of the ballistic system. The equation of state utilizes the Noble-Abel equation to give a description of the thermodynamic behavior of the propellant's gases. The Noble-Abel equitation is reasonably accurate for calculating the state of propellant's gases at high temperatures and density in a ballistic system (Johnston, 2005). Equation (21) represents the Noble-Abel equitation (Moreno, 2009):

$$\bar{P} = \frac{T}{V_c}\left[\sum_{i=1}^{n}\frac{F'_i C_i Z_i}{T_{0i}} + \frac{F'_I C_I}{T_{0I}}\right], \tag{21}$$

Where:

V_c Volume behind projectile available for propellant gas,

The Noble-Abel equitation requires the chamber volume. However, the chamber volume, in the ballistic system, is not constant due to propellant charge combustion and projectile motion. As the projectile start to move, the volume of the chamber start to increase. Also, as the propellant charge shrinks due to burning, the volume of the chamber also increases. Figure 18 illustrates chamber volume enlargement during the interior ballistic cycle. The initial chamber volume is represented as V_0, and V_c represents the total chamber volume after projectile displacement. As a result, $\mathrm{V}_c - \mathrm{V}_0$ represents the chamber volume enlargement due to projectile displacement.

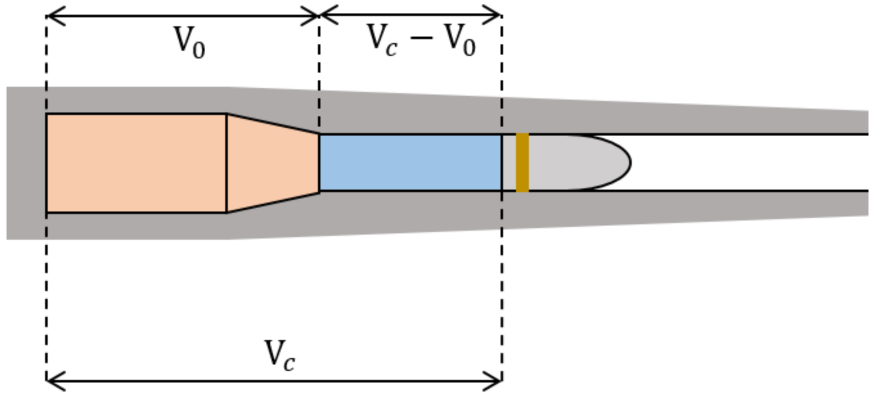

Figure 18: Chamber of ballistic system

Equation (22) is used to update the chamber volume during the interior ballistic cycle and it is expressed as (Moreno, 2009):

$$V_c = V_0 - \sum_{i=1}^{n} V_{P_i} + Ax - \sum_{i=0}^{n} \frac{C_i}{\rho_i}(1 - Z_i) - \sum_{i=0}^{n} C_i b_i Z_i - C_I b_I \ , \qquad (22)$$

Where:

x Projectile displacement,

V_0 Volume of empty gun chamber,

V_{P_i} Volume of parasitics associated with i^{th} propellant,

ρ_i Density of i^{th} propellant,

b_i Covolume of i^{th} propellant,

b_I Covolume of igniter,

Figure 19 shows the flowchart of the equation of state.

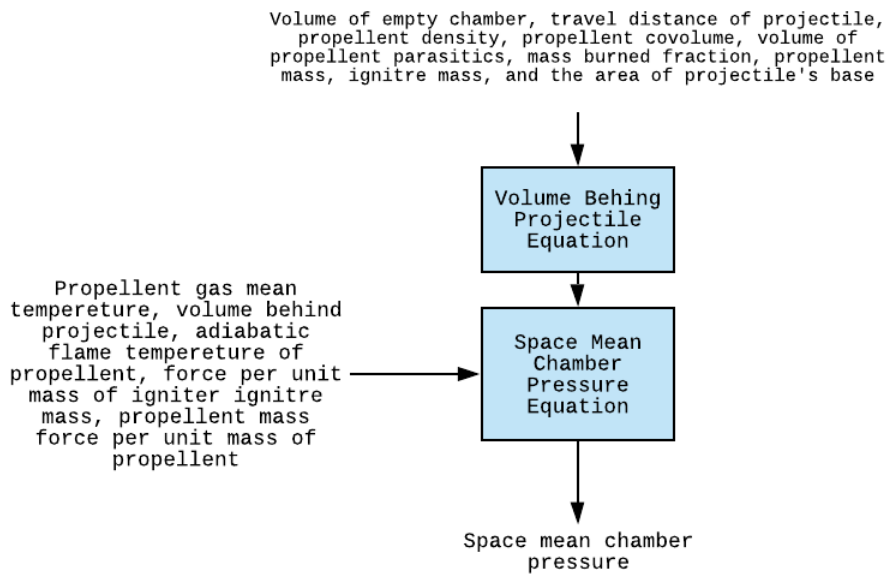

Figure 19: Flowchart of equation of state

Before calculating the space-mean pressure of the chamber, the volume of the chamber has to be updated. The volume of the chamber, consequently, is updated by the chamber volume equation. Then, the Noble-Abel equitation calculates the space-mean pressure of the chamber and passes it to the pressure gradient model.

2.3.4 Pressure gradient model

As the projectile starts to accelerate, it produces an expansion wave that starts to travel toward the breech. As the expansion wave impacts the breech, it reflects back to the projectile's base as a rarefaction wave. At this moment, the base-to-breech pressure ratio is almost one. However, when the rarefaction wave hits the projectile base and reflects back, the base-to-breech pressure ratio start to reduce, causing a reduction in the propellants gases' acceleration and gases' kinetic energy. This process is repeated in a continuous pattern throughout the interior ballistic cycle. The pressure at the projectile's base is always lower than the pressure at the breech due to the significant difference in velocities (Hansen & Heiney, 1987) (Jedlicka & Beer, 2007). Figure 20 is a schematic illustration of pressure gradient phenomenon during the interior ballistic cycle.

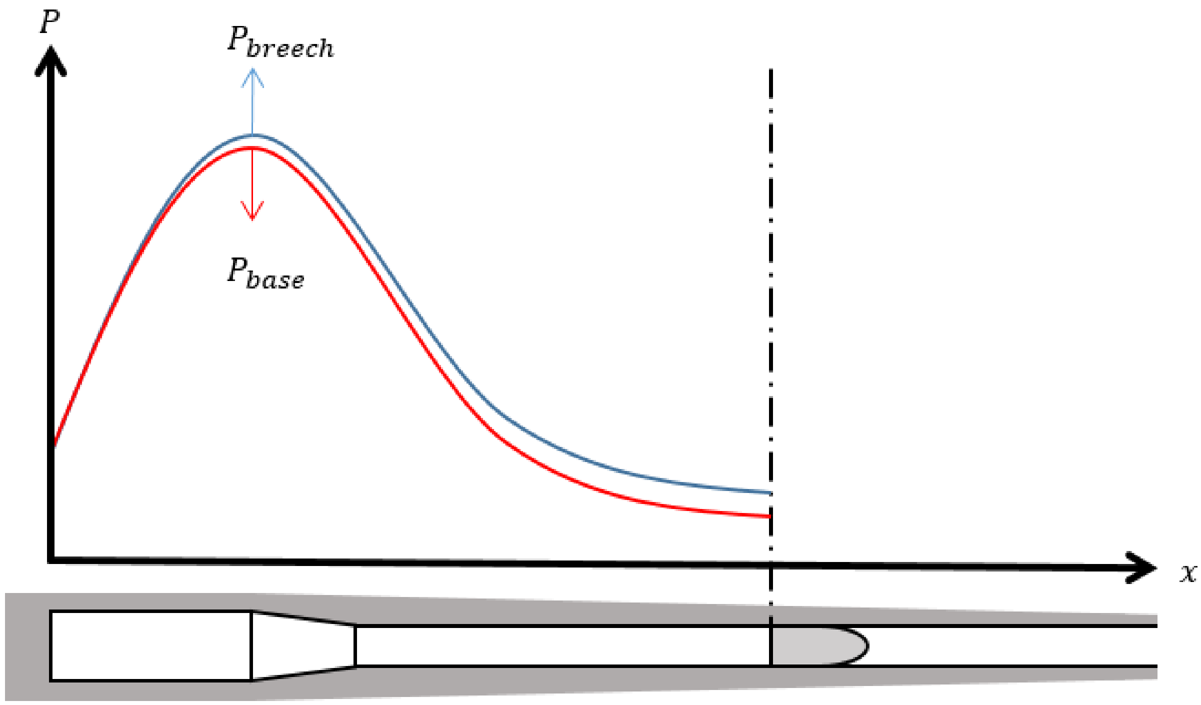

Figure 20: Pressure gradient profile

It can be seen that the pressure at the projectile's base is lower than the pressure at the breech and this is due to the pressure gradient phenomenon.

The most known model among ballisticians that solves the pressure gradient phenomenon is the Lagrange gradient model. The Lagrange gradient model is proposed as the approximated solution of the Lagrange ballistic problem, which is basically the problem of a piston being pushed by means of expanding gases released by rapid combustion. According to Morrison (1993), the Lagrange gradient model assumes the gas density between the breech and projectile's base is uniform. This results in a linear distribution of the gas velocity from the breech to the projectile's base. The Lagrange gradient model also assumes that the chamber of the ballistic system has the same diameter as the barrel. In addition, it assumes the propellant is instantaneously combusted prior to the projectile's motion. This leads to ignoring the fact that propellant grains flow with the moving gases. The Lagrange gradient model strongly depends on the ballistic ratio where the ratio is independent of projectile trajectory. When the ballistic ratio is small, the Lagrange gradient model is applicable. Nevertheless, when the ballistic ratio exceeds two, the Lagrange gradient model gives reasonable results since the model assumes the gas density from the breech to the base of the projectile is uniform. The Lagrange gradient model is the relation between base pressure, and breech pressure (Morrison & Wren, 1993).

The pressure on the base of the projectile (P_b) including the approximate pressure-gradient effect is (Morrison & Wren, 1993):

$$P_b = \frac{\bar{P}}{1 + \frac{\varepsilon}{3}} \ , \tag{23}$$

Where:

ε Ballistic mass ratio,

Ballistic mass ratio is:

$$\varepsilon = \frac{C}{m_p} \ , \tag{24}$$

The breech pressure (P_0) is:

$$P_0 = P_b \left(1 + \frac{\varepsilon}{2}\right), \tag{25}$$

However, there are several downsides of the Lagrange gradient model. The Lagrange gradient model neglects the fact that the projectile experiences a resistive pressure due to driving band engraving and friction. In addition, it neglects the fact that the projectile experiences resistive pressure due to air compression ahead of projectile during acceleration. As a result, the Lagrange gradient model is improved to take into account the resistive pressure that the projectile experiences while accelerating due to engraving and barrel friction. In addition to that, the model improved to take the air pressure in front of the projectile into account (Gronheim, 2000) (Anderson, 1987). The improved Lagrange model as represented in STANAG 4367 is expressed as:

The pressure on the base of the projectile (P_b) including the approximate pressure-gradient effect is (Gronheim, 2000):

$$P_b = \frac{\left[\bar{P} + \frac{C_T\left(P_g + P'_R\right)}{3m_p}\right]}{\left[1 + \frac{C_T}{3m_p}\right]}\ , \qquad (26)$$

Where:

P_g Pressure of gas or air ahead of projectile,

The breech pressure (P_0) is:

$$P_0 = P_b + \frac{C_T}{2m_p}\left(P_b - P'_R - P_g\right), \qquad (27)$$

Figure 21 illustrates the flowchart of the pressure gradient model.

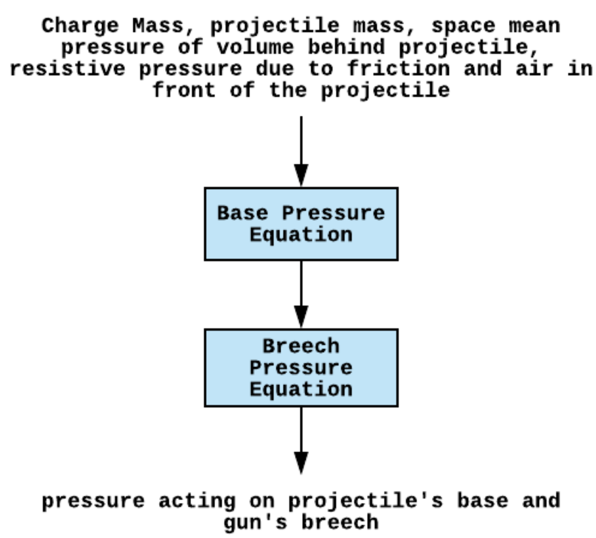

Figure 21: Flowchart of pressure gradient model

After the space-mean pressure is calculated, the base pressure equation calculates the exerted amount of pressure on the projectile's base. Then, the breech pressure equations solves the amount of pressure exerted on the gun's breech.

2.3.5 Equation of motion

The equation of motion calculates the acceleration, velocity, and displacement of projectile and gun during the interior ballistic cycle. When the propellant charge is ignited and the pressure starts to build up, tremendous force is exerted on the projectile's base and gun's breech. As a consequence, the projectile tends to accelerate forward and the gun tends to accelerate in the opposite direction. The equation of motion is governed by Newton's second low. The net forces acting on the projectile and the gun during interior ballistic cycle are illustrated in Figure 22:

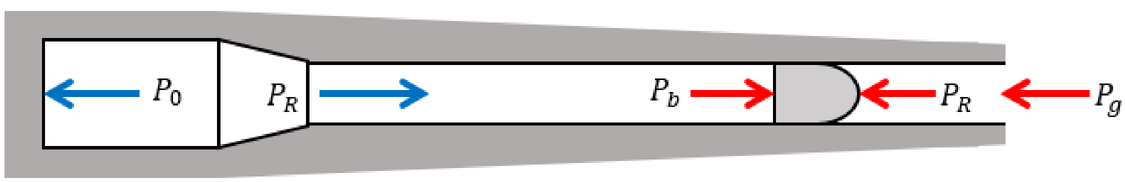

Figure 22: Net forces acting on the projectile and the gun

The net forces acting on the gun and their directions are highlighted in blue arrows. They are the forces due to breech pressure and resistive pressure. The forces that act against the projectile motion are always negative. As a result, the acceleration of the center of mass of the recoiling gun (v_{rp}) is provided by Equation (28) (Moreno, 2009):

$$\dot{\boldsymbol{v}}_{\boldsymbol{rp}} = -\frac{A_{br}P_0 - AP'_R}{m_{rp}}, \tag{28}$$

Where:

A_{br} Area of breech face,

The negative sign reflects the direction of motion. When the acceleration is calculated, the gun velocity and displacement can be found. The velocity of the gun recoiling (v_{rp}) in the earth reference frame is calculated as (Moreno, 2009):

$$v_{rp} = \int_0^{t_r} \dot{v}_{rp} dt_r , \tag{29}$$

Where:

t_r Recoil time,

The displacement of the gun due to recoiling (x_{rp}) in the earth reference frame is calculated as:

$$x_{rp} = \int_0^{t} v_{rp} \, dt , \tag{30}$$

Similarly, the net forces acting on the projectile and their directions are highlighted in red arrows. They are the forces due to base pressure, resistive pressure due to air in front of the projectile, and resistive pressure due to driving band engraving and friction. The direction of each force is clearly shown in Figure 22. As a result, equation (31) provides the equation of acceleration of the center of mass of the projectile (Moreno, 2009):

$$\dot{\boldsymbol{v}}_{\boldsymbol{p}} = \frac{A(P_b - P'_R - P_g)}{m_p}, \tag{31}$$

Where:

P_b Pressure on base of projectile,

f_r Down-tube resistance factor,

P'_R Adjusted resistive pressure of the bore due to friction and engraving,

m_p Mass of projectile,

A Area of base of projectile including appropriate portion of rotating band, The area of the base of the projectile, including the appropriate portion of the rotational band, is described by (Moreno, 2009):

$$A = \frac{\pi}{4} D_b^2 \,, \tag{32}$$

Where:

D_b Diameter of bore,

If the bore is smooth, the diameter would be easily determined. If the bore is rifled, however, the bore diameter is determined differently because of the presence of the circumferential grooves in the bore. Before representing the equation of calculating the diameter of the rifled bore, it is important to understand the rifled bore further. Figure 23 shows a cross-sectional image of a rifled bore.

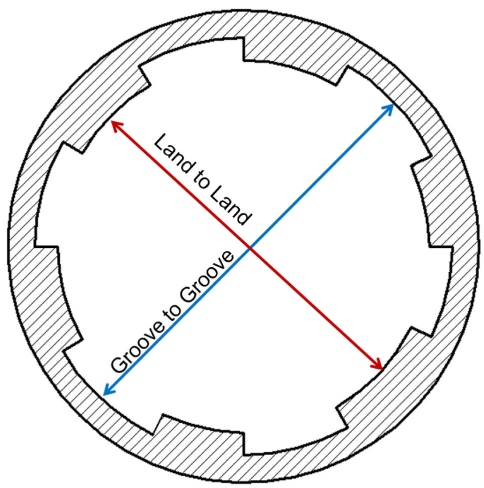

Figure 23: Cross-section of rifled bore

As can be seen, the rifled bore’s internal surface is not uniform due to the grooves and lands. According to STANAG 4367, the diameter of rifled bore is calculated as (Moreno, 2009):

$$D_b^2 = \left[\frac{GLR * DG^2}{GLR + 1} + \frac{DL^2}{GLR + 1}\right], \tag{33}$$

Where:

GLR Groove to land width ratio,

DG Diameter of lands,

DL Diameter of groove,

After the projectile acceleration is calculated, the velocity of the center of mass of the projectile is given by (Moreno, 2009):

$$v_p = \int_0^t \dot{v_p}\, dt \,, \tag{34}$$

Where:

t Time,

As the projectile and the gun are moving apart, the relative displacement of the projectile to the gun is equal to the projectile displacement plus the gun displacement. As a result, the projectile displacement is expressed as (Moreno, 2009):

$$x = \int_0^t v_p\, dt + \int_0^t v_{rp}\, dt \,, \tag{35}$$

Where:

v_{rp} Velocity of recoiling parts is always negative,

Figure 24 illustrates the flowchart of the equation of motion.

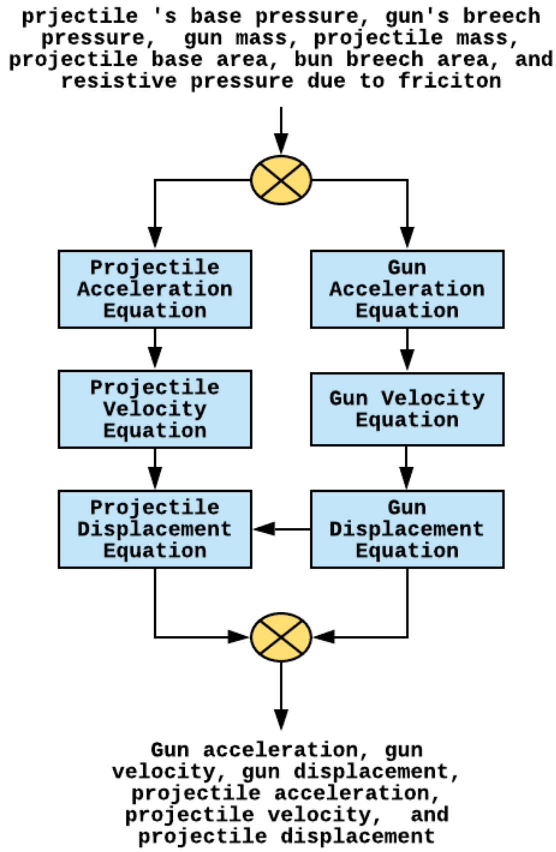

Figure 24: Flowchart of the equation of motion

When the projectile's base pressure and gun's breech pressure are available, the acceleration of the gun as well as the projectile can be calculated using equation (28) and equation (31). Then, the velocity of the gun and projectile can be found by integrating the acceleration. Before calculating the projectile's displacement, the displacement of the gun has to be calculated. Thus, the position of the projectile can be calculated.

2.3.6 Utilized assumptions by the LPM of STANAG 4367

When simulating a ballistic system using the LPM of interior ballistics, there will be an error due to the use of the following assumptions:

- LPM assumes all propellant grains and elements are identical in terms of physical and chemical properties.
- During ignition, LPM assumes all loaded propellant grains and elements are ignited instantaneously and simultaneously.
- During combustion, LPM assumes combustion takes place at constant speed on all propellant grains burn in parallel layers.
- LPM assumes the combustion takes place in a well-mixed reactor.
- LPM imposes space-mean pressure to calculate the burn rate of propellant grains and elements.
- As the projectile travels through the barrel, LPM assumes there is no gas leakage between the projectile and the bore. In other words, it assumes the rotational band prevent any gas leakage.
- The projectile has a constant mass.
- The base of the projectile is assumed to be flat and the base force is distributed uniformly.
- LPM assumes that the chamber has the same diameter as the bore. So, if there is any chambrage in the ballistic system, it is neglected.
- LPM assumes that the density, temperature, and pressure of the propellant gases are uniform along the ballistic system.

Not all these assumptions hold true. There is consequently always a slight error between the calculated and measured values (Antonie, 2013) (Dyckmans, 2015).

2.3.7 Calibration of the LPM of STANAG 4367

Because of the utilized assumption of the LPM of interior ballistics, there is a difference between the experimental and the computational muzzle velocity and maximum chamber pressure. The differences can also be due to error of data related to projectile, gun, and propellant charge. The problem is solved by adding calibration factors or fitting factors to the equations containing data prone to errors. The fitting factors are to adjust or calibrate the LPM of interior ballistics and to force it within acceptable margins. Thus, LPM of interior ballistics can be used to make reasonably good predictions. The value of the fitting factor ranges between 0.1 and 1. However, the value of the fitting factor should be close to 1, or else the LPM of interior ballistics will not be applicable (Dyckmans, 2015) (Moreno, 2009). There are four fitting factors in the LPM of STANAG 4367 to calibrate it to the experimental data. These fitting factors are:

- The burn rate factor (f_β) and burning rate temperature factor ($f_{\beta T}$):

  These factors aid to match the computational maximum chamber pressure of the ballistic system to the measured maximum chamber pressure. The burn rate factor is used to modify the value of the burn rate exponent and coefficient. It is difficult to determine the burn rate exponent and coefficient with 100% accuracy. As a result, the burn rate factor is used to adjust the value of the burn rate coefficient and exponent. Conversely, the burning rate temperature factor is used to modify the temperature of the propellant charge. Equation (36) is the burn rate equation after including the mentioned fitting factors (Moreno, 2009):

$$r_i = f_\beta f_{\beta T} \beta_i (\bar{P})^{\alpha_i} , \tag{36}$$

- The force temperature factor (f_{FT}):

  This factor aids to match the computational muzzle velocity of the ballistic system to the measured muzzle velocity. The force temperature factor is used to modify the value of the force constant of the propellant as it cannot be determined with 100% accuracy. Equation (37) is the propellant force per unit mass after including the mentioned fitting factors (Moreno, 2009):

$$F'_i = f_{FT} F_i , \tag{37}$$

Where:

F_i Force per unit mass of i^{th} propellant,

- The down-tube resistance factor (f_R):

  This factor aids to match the computational muzzle velocity of the ballistic system to the measured muzzle velocity. To determine the down-tube resistance of a ballistic system is one of the biggest challenges that ballisticians face. As a result, the down-tube resistance factor is used to modify the value of the down-tube resistance. Equation (38) is the resistive pressure after including the mentioned fitting factors:

$$P'_R = f_R P_R , \tag{38}$$

Where:

P_R Resistive pressure of the bore due to friction and engraving,

2.4 Alternative Heat transfer model

In order to determine the available energy of propellant gas during combustion as realistically as possible, it is crucial to accurately calculate the amount of heat transferred from propellants' gases to the gun. Heat transfer calculations play a vital role in the accuracy of an interior ballistic simulation. The calculation of heat transfer rate is based on the heat flux equation for gas to solid surface transfer. The heat flux equation, equation (39), forms the heart of the heat transfer model and it is expressed as (Moreno, 2009):

$$Q = A_w h(T - T_c)\ , \tag{39}$$

Where:

Q	The rate of heat transfer,
A_w	Chamber wall area plus area of gun tube wall exposed to propellant gases,
h	Convective heat transfer coefficient,
T_c	Temperature of chamber wall,
T	Propellant gas mean temperature,

The variation on the heat flux equation can only be done on the method of determining the convective heat transfer coefficient and the methodology of calculating the chamber wall temperature.

The method of STANAG 4367 of calculating the temperature of the chamber wall is not suitable for a 155 mm artillery system, which is noticed during work routines. The temperature of the chamber wall equation of STANAG 4367 strongly depends on the nominal wall thickness. However, a 155 mm artillery system does not have a uniform wall thickness. Thus, it is challenging to determine an accurate nominal wall thickness for a 155 mm artillery system to result in an accurate chamber wall temperature calculation. The heat flux equation consequently generates inaccurate results, which significantly influences the accuracy of the LPM of STANAG 4367. The following is an alternative methodology to calculate the chamber wall temperature.

2.4.1 Chamber wall temperature:

The Ballistic Research Laboratory of US Army developed a two-dimensional model to simulate the interior ballistic cycle of a ballistic system (Gough, 1983). In the two-dimensional model, a one-dimensional equation is proposed to calculate the surface temperature of solid propellants according to the cubic temperature profile in penetration distance (Gough, 1983). It would be considered that this solution is applicable to the chamber wall. Unfortunately, the one dimensional equation and the cubic profile approximation are not discussed explicitly in the reference. The positive aspect about the one-dimensional equation is that it does not take into account the chamber wall thickness. After adapting the method to calculate the chamber wall temperature, it is expressed as in Equation (40) (Gough, 1983):

$$\Delta T_c = \frac{-h2 * E_h + \sqrt{(h2 * E_h)^2 - 4.0 * 0.75 * \rho_w * C_{pw} * k * A_w * \; - E_h * \left(h1 * T - h2 * T_{0_w}\right)}}{\left(2.0 * 0.75 * \rho_w * C_{pw} * k * A_w\right)}, \quad (40)$$

Where:

k Heat Conductivity of the gun,

$h1$ Convective heat transfer coefficient of propellant gas,

$h2$ Convective heat transfer coefficient of chamber wall,

The chamber wall temperature is determined as (Gough, 1983):

$$T_c = \Delta T_c + T_{0_w}, \quad (41)$$

2.4.2 Convective heat transfer coefficients

There are several convective heat transfer coefficients which are developed specifically for ballistic system applications. It is worthwhile to include a few other coefficients in the investigation other than the coefficients of STANAG 4367. The following sections represent a few convective heat transfer coefficients, which are developed for ballistic system application.

2.4.2.1 Gough’s coefficient

Gough’s coefficient is represented in a two-dimensional model of interior ballistics that was proposed by the Ballistic Research Laboratory of US Army (Gough, 1983). Gough’s coefficient is governed by the empirical correlation of Gelperin and Einstein. In Gough’s coefficient, the gas dynamic viscosity is evaluated at film temperature, which is an approximation to the temperature of propellant gas inside a convection boundary layer. The Gough's method is represented below (Gough, 1983) (Singh, 2009):

$$h_1 = h_2 = \frac{0.0288 * k_{gas} * R_e^{0.8} * P_r^{0.33}}{0.5 * \left(\frac{V_c}{A} * x\right)}, \tag{42}$$

Where:

R_e Reynolds number,

P_r Prandtl number,

k_{gas} Gas Thermal conductivity,

The Reynolds number is given by (Gough, 1983):

$$R_e = \frac{\rho u d}{\mu}, \tag{43}$$

Where:

ρ Propellant gas density,

u Propellant gas velocity,

μ Propellant gas dynamic viscosity,

d Propellant gas travel distance,

The gas dynamic viscosity is provided by (Gough, 1983):

$$\mu = 0.0134064 * \frac{\left(\frac{T}{298}\right)^{1.5}}{T + 110.0}, \tag{44}$$

Prandtl number is provided by (Gough, 1983):

$$P_r = \frac{4 * \gamma}{9 * \gamma - 5}, \tag{45}$$

Where:

γ Ratio of specific heats for propellant gas,

2.4.2.2 Lawton's Coefficient

Lawton and Laird developed a semi-empirical convective heat transfer coefficient to account for initial barrel temperature (Johnston, 2005). The coefficient of Lawton becomes useful for a repeated firing application. It is claimed that the accuracy of the heat transfer model using the coefficient of Lawton is approximately 8% (Johnston, 2005). The coefficient of Lawton depends on Reynolds number, which is a measure that determines the gas flow type; whether it is turbulent or laminar. It also depends on a few other factors such as the thermal conductivity of the gas and gas travel length. The convective heat transfer coefficient of propellant gas and the convective heat transfer coefficient of chamber wall are represented below (Johnston, 2005):

$$h_1 = \frac{k_{gas}}{x} * 0.85 * R_e^{0.7} , \tag{46}$$

$$h_2 = h_1 + \frac{k_{gas}}{l} * 2000 * E_{exp} , \tag{47}$$

Where:

E_{exp} Expansion number,

l Characteristics gas travel length,

R_e Reynolds number,

The expansion number is a non-dimensional number and it is determined as in Equation (48) (Johnston, 2005):

$$E_{exp} = \frac{\gamma - 1}{V_s} \frac{dV}{dt} \left(\frac{C * C_v * l^3}{k_{gas} * V_0 * u_{base}} \right)^{0.5} , \tag{48}$$

Where:

C_v The mixture specific heat at constant volume,

V_s The volume occupied by propellant gas,

u_{base} The gas velocity at the base of the projectile,

2.5 Possible variations of heat transfer model

As was mentioned, the heat transfer model can only be varied by manipulating the convective heat transfer coefficient and the method of calculating the chamber wall temperature. Consequently, based on the previous section, three possible variations of heat transfer model can be formulated. They are provided by:

1. Using the convective heat transfer coefficient of STANAG 4367 and the one-dimensional equation of calculating the chamber wall temperature.
2. Using the convective heat transfer coefficient of Gough and the one-dimensional equation of calculating the chamber wall temperature.
3. Using the coefficient of Lawton and the one-dimensional equation of calculating the chamber wall temperature.

These variations has to be investigated and compared to the heat transfer model of STANAG 4367. Their negative or positive effects on the lumped parameter of STANAG 4367 have to be observed.

2.6 Conclusion

In this chapter, the interior ballistic cycle and the LPM of STANAG 4367 were described in more detail. The assumptions utilized by the LPM of STANAG 4367 were outlined. The fitting factors to calibrate the LPM of STANAG 4367 were also described. The heat transfer model of the LPM was discussed. An alternative equation for calculating the chamber wall temperature as well as heat transfer coefficients were proposed. Three possible variations of the heat transfer model were formulated to be investigated and whether they are better alternative than the heat transfer model of STANAG 4367.

Chapter III Methodology

3.1 Introduction

In the previous chapter, the LPM of STANAG 4367 was described. Three variations of the heat transfer model were established as alternatives to the heat transfer model of STANAG 4367. In this chapter, the LPM simulation program is going to be developed. The three variations of the heat transfer model would be included in the simulation program and the program would be able to switch between the variations of heat transfer model. The purpose of the simulation program is to serve the main aim of this research, which is to find the most suitable heat transfer model for simulating a 155 mm artillery system. The LPM of interior ballistics simulation program would be verified against RDM's interior ballistics simulation program.

3.2 Development of the LPM simulation program

The development of the LPM simulation program will be implemented in three stages.

1. A pneumatic gas gun simulation program will be developed. A pneumatic gas gun uses compressed gas to propel projectiles. The program will be verified against the analytical model of a pneumatic gas gun.

2. The combustion model and pressure gradient model will be lumped to the pneumatic gas gun simulation program. The energy model of the pneumatic gas gun simulation program will be updated according to STANAG 4367. At this stage, the simulation program would be STANAG 4367 compliant. The simulation program will be verified against the interior ballistic simulation program of RDM.

3. The above-mentioned simulation program would be expanded to incorporate the different variations of the heat transfer model, which was described in Sections 2.4 and 2.5. Each heat transfer model variation will be verified by making sure there is no oscillation or discontinuity in the result obtained via the variation itself. After verification, the model will be ready to perform the investigations, which aims to find the most suitable heat transfer model for simulating a 155 mm artillery system.

3.2.1 Programming language

The LPM simulation program will be compiled in MATLAB. MATLAB has a comprehensive, integrated development environment (IDE). The MATLAB IDE has vast capabilities, which makes it very useful for iterative workflows and applications.

3.2.2 Accuracy

The accuracy of the simulation program is influenced primarily through rounding errors and truncation errors. A rounding error is due to rounding off of the result(s) obtained by an algorithm. Rounding errors cannot be controlled as they are associated with floating-point arithmetic, which computers use to perform the calculations.

Truncation errors center on the numerical method and time intervals or time steps. A truncation error can be defined as the difference between the approximated solution of the numerical model and the exact solution. If the solution is approximated through a numerical method, the truncation error cannot be eliminated. It would still exist even if the rounding errors were absent. However, truncation errors can be controlled with appropriate numerical methods and time intervals.

3.2.2.1 Numerical method

As was explained above, truncation errors can be controlled by selecting the appropriate numerical method and time intervals. The truncation error becomes high when first-order numerical methods are used, but it becomes less with higher order numerical methods are employed. The difference between higher order and lower order numerical methods is that lower order numerical methods, such as the Euler method, use the information on the slope or the derivative of an integral at the given time step to extrapolate the solution to the next time-step. They also require less computational processes in order to generate the answer. Higher order methods, such as the Runge-Kutta forth order method and Euler pre-corrector method, use the information on the slope at more than one point to extrapolate the solution to the future time step. They also require more processing in order to generate the answer (Press, 2002).

The selected numerical method for this application is the Euler method. It is a first order numerical integration method and is the simplest, most explicit integration method. The truncation error of the Euler method is proportional to the time intervals. Furthermore, it is fast, robust, and proven to be good enough for such an application (Schabort, 2016).

3.2.2.2 Time intervals

Time intervals play a vital rule in the truncation error and the resulting accuracy of the simulation program. The truncation error of the Euler method is proportional to the time intervals. The duration of the interior ballistic cycle is approximately 15 milliseconds. When the time interval is 1 millisecond, which is relatively large, the truncation error becomes large. When the time interval is 0.001 millisecond, which is relatively small, the truncation error becomes smaller. However, when the time intervals are small, it acquires longer computational time. As a result, the computation cost increases, which lowers the efficiency of the simulation program. Consequently, it is important to select the right time interval that offers a good balance between the accuracy and the cost of computations. An optimal time interval would be decided in the section that follows when the LPM simulation program is completely developed. Currently, the time intervals that are chosen for the purpose of program development, is 0. 001 millisecond.

3.2.3 Program algorithms

The purpose of an algorithm is to compile a sequential set of logical steps to solve a particular problem. In other words, it is to establish a procedure to solve a mathematical or computational problem. An algorithm can include calculations, reasoning, or data processing. Today, algorithms are intensively used in model development to greatly improve work efficiency. It has become an essential part of model development. An algorithm can be represented via different forms that can either be flowchart or pseudo code. Flowcharts are considered an obvious method to represent an algorithm and offers a visual representation of algorithm. Program algorithms will be presented by means of flowchart.

3.2.4 Stage one of LPM simulation program development

At this stage, the pneumatic gas gun simulation program forms the fundamental base of the full LPM simulation program. The current program is not sufficiently mature to simulate a conventional ballistic system, yet sufficiently mature to simulate a pneumatic gas gun. A pneumatic gas gun uses compressed gas to propel projectiles. In other words, no propellant combustions are involved. The current program includes the energy model, equation of state, and equation of motion as stated in STANAG 4367. However, it excludes the combustion models, which simulate propellant combustions. It also excludes the pressure gradient model. The flowchart of the pneumatic gas gun simulation program is illustrated Figure 25.

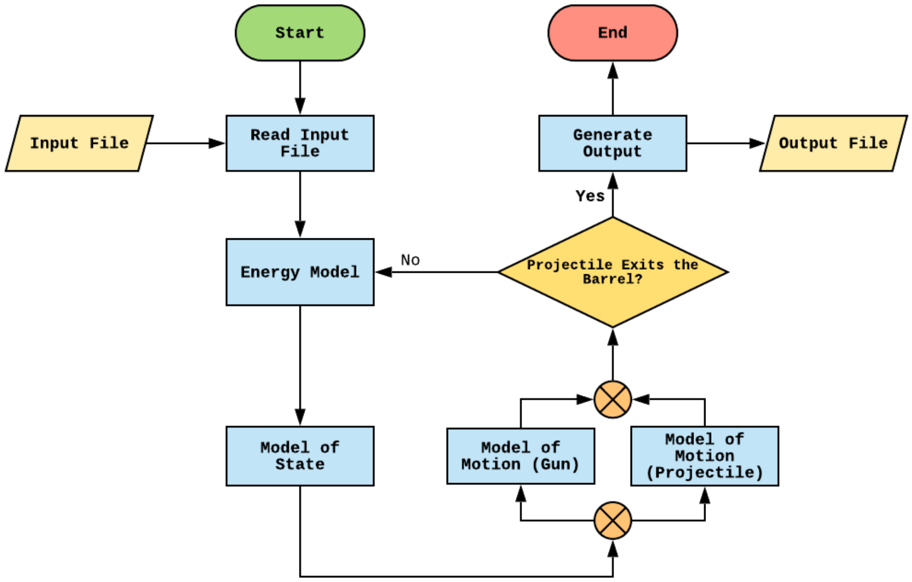

Figure 25: Pneumatic gas gun flowchart

The program starts by reading all the inputs. The available energy in the compressed gas is calculated through the energy model and the result is passed to the equation of state. The equation of state calculates the space-mean pressure. In the current program, the pressure gradient model is not included yet. As a result, the base and breech pressure of the projectile and the gun are equal to the space-mean pressure. The space-mean pressure is passed to the equation of motion to solve the acceleration, velocity, and displacement of the projectile and gun. After that, the state of the projectile is checked via the program. If the projectile exits the muzzle, the output is generated and the program is terminated. However, if the projectile has not exited the muzzle yet, the program will loop until the condition is met.

3.2.4.1 Program verification

Program verification is conducted to determine whether or not the program is accurately implemented and accurately represents the developer's conceptual description and specifications (Bingue, 2018). The current model underwent two stages of verification, which include the following:

1. The first stage is by visually examining the generated outputs of the pneumatic gas gun simulation program and making sure there are neither oscillations nor discontinuities in the generated outputs.
2. The second stage is by comparing the outputs of the simulation program of pneumatic gas gun against the outputs of the analytical model of pneumatic gas gun.

In the current simulation program, a few outputs variables have to be examined to ensure that the program is correctly implemented, which are the following:

- Chamber pressure,
- Gas temperature,
- Projectile acceleration,
- Projectile velocity, and
- Projectile displacement.

While examining these variables, it is important to detect any sort of oscillations or discontinuities. Figure 26 shows the pressure curve generated by the pneumatic gas gun simulation program.

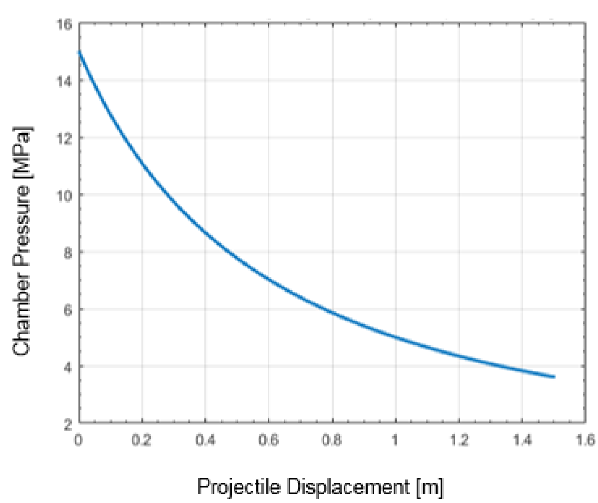

Figure 26: Chamber pressure [MPa] vs projectile displacement [m]

The initial chamber pressure of the simulated gas gun as 15 MPa. As the projectile starts moving in the barrel, the chamber's volume starts to increase. Because of the chamber's volume enlargement, the chamber pressure starts to reduce. It is noticeable that the pressure curve reflects the expansion process of the compressed gas within the chamber. As can be seen, the curve is smooth and free of any oscillations or discontinuities.

The expansion of the compressed gas caused the projectile to accelerate. Because the projectile acceleration is a function of the pressure curve, it is expected that the acceleration curve would correspond to the pressure curve. The first integration of the acceleration represents the projectile velocity and the second integration represents the projectile displacement. Figure 27 below represents the acceleration, velocity, and displacement curves of the projectile during the interior ballistic cycle of the pneumatic gas gun.

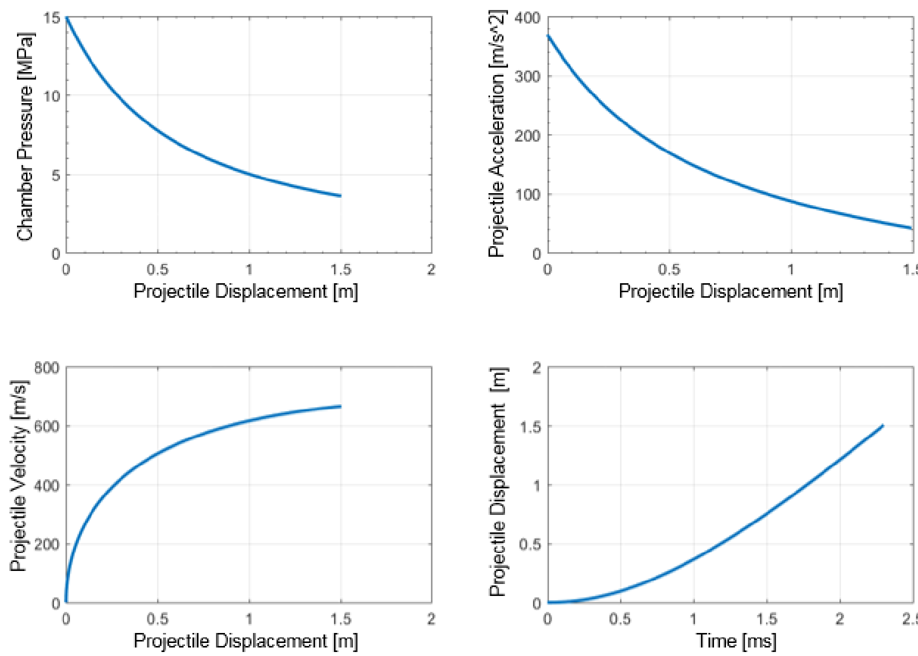

Figure 27: Projectile acceleration, velocity, and displacement

As can be seen from Figure 27, the curves are free of any oscillations or discontinuities. Figure 28 below shows the gas temperature during the interior ballistic cycle of the pneumatic gas gun. During interior ballistic cycle, the compressed gas starts expanding. The gas expansion causes the projectile to accelerate. Therefore, the compressed gas starts to lose energy. As the compressed gas start losing energy, its temperature starts to decrease.

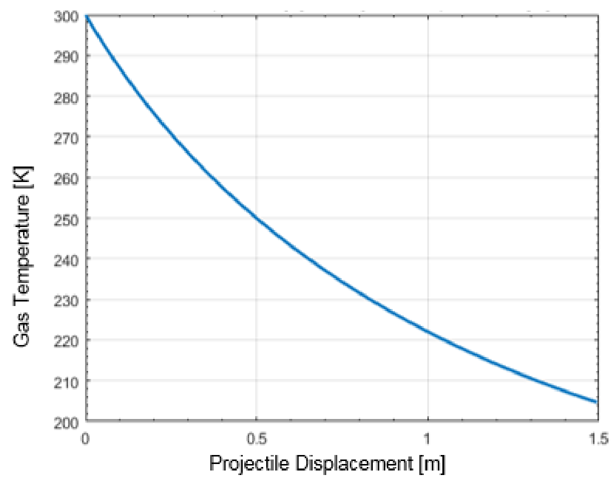

Figure 28: Gas temperature [K] vs projectile displacement [m]

As illustrated in Figure 28, the curve of the compressed gas temperature is free of any oscillations or discontinuities.

The generated outputs of the pneumatic gas gun simulation program are free of oscillations or discontinuities, which indicates that the simulation program is correctly implemented and free of errors. Now, the simulation program is ready to be verified against the analytical model of the pneumatic gas gun. The analytical model is represented by (Carlucci, 2007):

$$V_m = \sqrt{2 * \frac{m_g}{m_p} * \frac{R T_i {l_c}^{(\gamma-1)}}{(1-\gamma)} * \left[(l_c + L_b)^{(1-\gamma)} - {l_c}^{(1-\gamma)}\right]}, \tag{49}$$

Where:

V_m	Muzzle velocity,
m_g	Gas mass,
m_p	Projectile mass,
γ	Specific heat ratio of the gas,
R	The universal gas constant,
T_i	The absolute temperature,
l_c	Chamber length,
L_b	Barrel length,

The analytical model assumes that the gas behaves ideally. The gas is compressed within the chamber adiabatically. In addition, it assumes there is neither friction nor gas leakage between projectile and the barrel. However, it takes into account the projectile kinetic energy. It also calculates the projectile velocity as a function of its displacement. Figure 29 shows a comparison of the pressure curve, projectile velocity, and gas temperature between the analytical model, as well as the simulation program of the pneumatic gas gun.

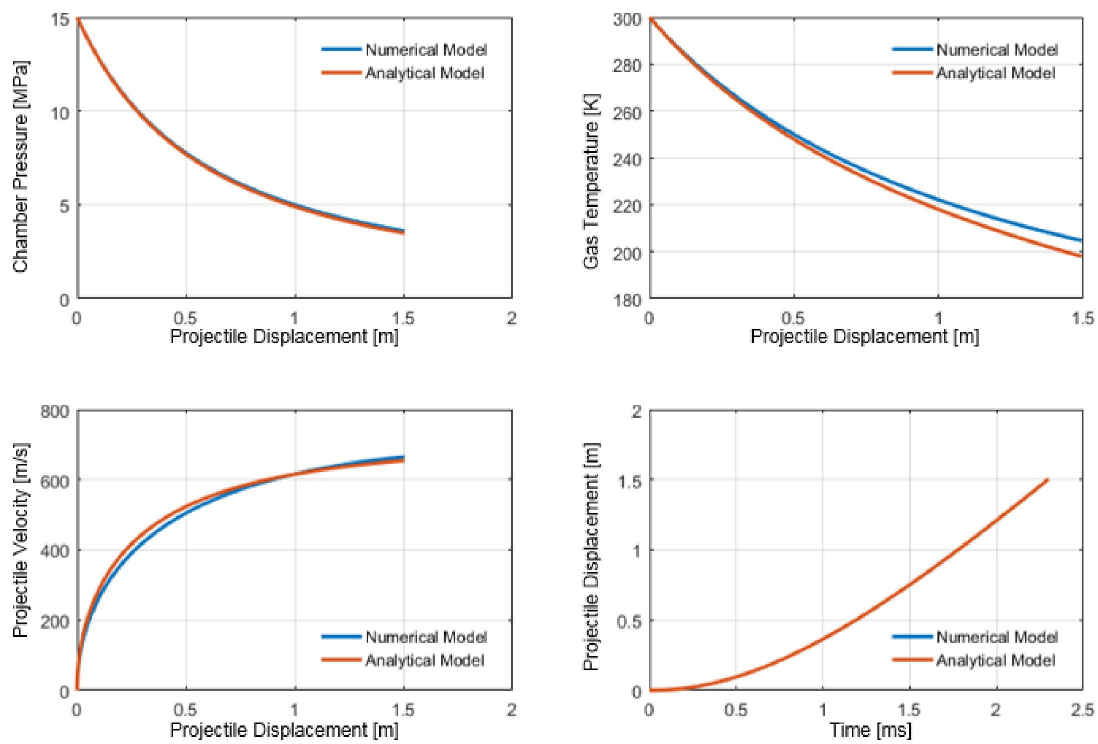

Figure 29: Outputs comparison

From the figure above, it can be seen that the simulation program is performing very well against the analytical model, and both models came almost to the same answers. Table 1 represents the outputs of both models.

Table 1: Developed program and analytical mode comparison

Pneumatic Gas Gun	Simulation program	Analytical model	Deviation (%)
Muzzle Velocity (m/s)	665.07	654.32	-1.6
Exit Pressure (MPa)	3.62	3.48	-3.8
Exit Gas Temperature (K)	95.30	102.03	7.1

Evidently, the deviation in the calculated muzzle velocity between the simulation program and analytical models is almost -1.6 percent (10 m/s). The deviation in the calculated exit pressure is almost -3.8 percent (0.15 MPa). The deviation in the calculated exit gas temperature is almost 7.1 percent (7 K). Unfortunately, there is no measured data for such a system to compare and analyze both models against. At this stage, the simulation program of the pneumatic gas gun is considered acceptable and mature for the next stage of the development, which is to expand it to be STANAG 4367 compliant.

3.2.5 Stage two of LPM simulation program development

In order for the pneumatic gas gun simulation program to be STANAG 4367 compliant, the combustion model, and pressure gradient model are lumped into it. In addition, the energy model is expanded to include the heat transfer model and the gas kinetics model. Figure 30 shows the flowchart of the LPM simulation program, which is the expanded pneumatic gas gun simulation program.

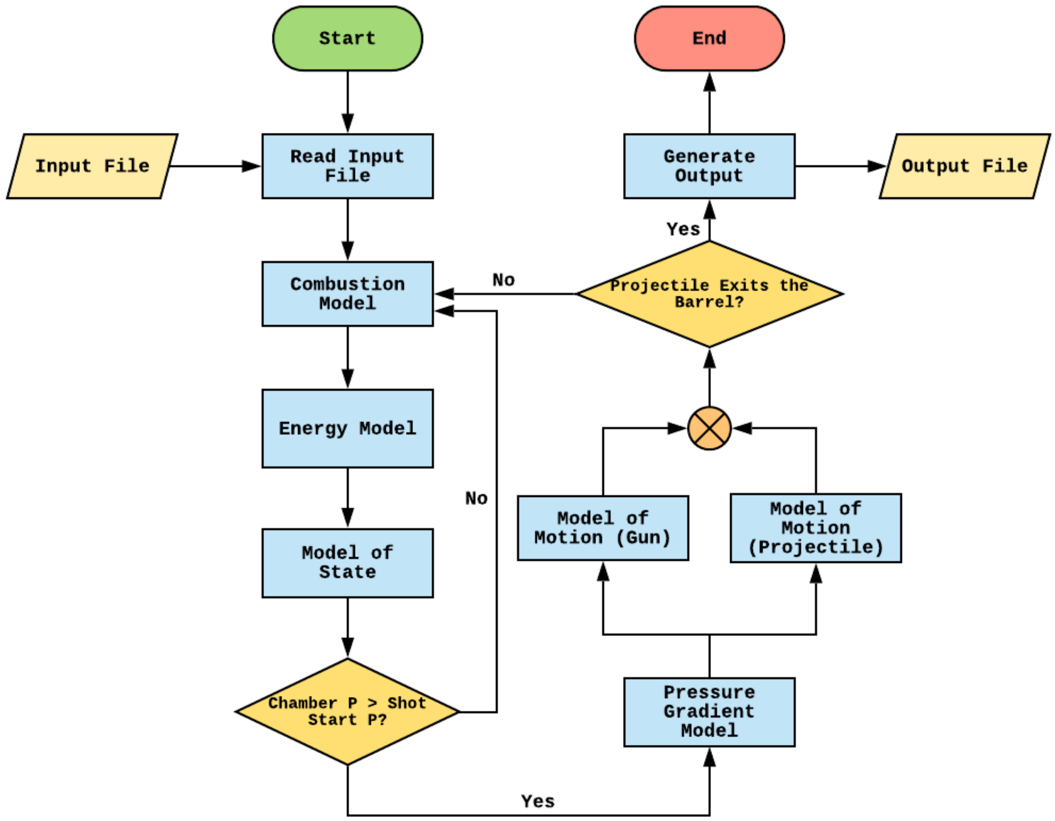

Figure 30: Flowchart of LPM of IB

1. The program starts by reading all the inputs.
2. The combustion model calculates the generated gas mass due to propellant burning and the remaining solid mass of the propellant.
3. The energy model calculates the available energy in the propellant gas and passes it to the equation of state to calculate the space-mean pressure.
4. The program checks the space-mean pressure if it is greater than the shot start pressure or not.
5. If the space-mean pressure is still less than the shot start pressure, the program will loop until the condition is met.
6. After the condition is met, the space-mean pressure is passed to the pressure gradient model to calculate the excreted pressure on the projectile base and gun breech.
7. After that, the equation of motion solves the acceleration, velocity, and displacement of the projectile and gun.

8. The projectile state is checked via the program. If the projectile exits the muzzle, the outputs are generated and the program is terminated. However, if the projectile has not exited the muzzle, the program will loop until the condition is met.

3.2.5.1 Model verification

The current LPM simulation program underwent two stages of verification, which are as follows:

1. The first stage is by visually examining the generated outputs of the current LPM simulation program and making sure there are neither oscillations nor discontinuities in the generated outputs.
2. The second stage is by comparing the outputs of the simulation program against the outputs of the interior ballistic simulation program of RDM.

In the current model, a few output variables have to be examined to ensure that the model is correctly implemented, which are the following:

- Chamber pressure,
- Gun’s breech pressure,
- Projectile’s base pressure,
- Projectile acceleration,
- Projectile velocity, and
- Projectile displacement.

The main outputs of the LPM simulation program are shown in Figure 31 after simulating a 155 mm artilary system. The simulated 155 mm artilary system will be described further in Chapter 4. in Figure 31 , The outputs are pressure curves,which include the space-mean pressure, projectile’s base pressure, and gun’s breech pressure, projectile acceleration, projectile velocity and displacement.

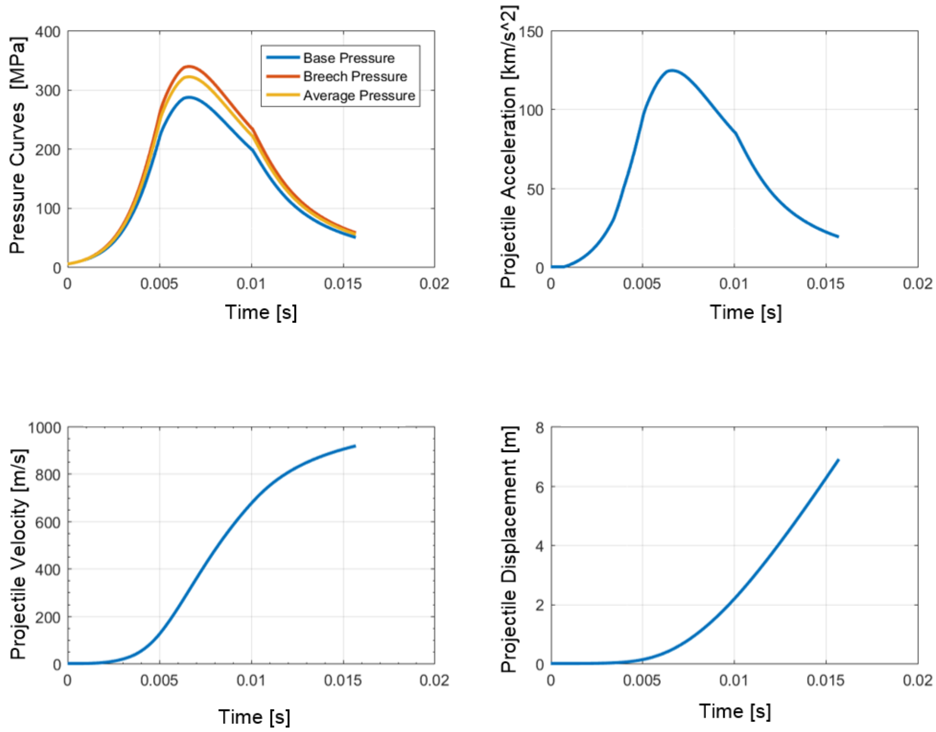

Figure 31: Pressure, projectile acceleration, velocity, and displacement curves

The breech, base and space-mean pressure curves are shown in Figure 31. It can be seen that due to the presence of a propellant charge, there is an increase of pressure inside the gun chamber. The difference between breech, base and space-mean pressure is due to the pressure gradient phenomenon. Because the projectile acceleration is a function of the base pressure, it is expected that the acceleration curve would correspond to the pressure curve. The first integration of the acceleration represents the projectile velocity and the second integration represents the projectile displacement. All the curves shown in Figure 31 are free of any discontinuities or oscillations. It indicates that the program is implemented correctly and free of errors.

Now, the program is ready to be verified against RDM’s IB simulation program. However, before verifying the developed program against RDM’s IB simulation program, it is crucial to select the right time interval that offers an acceptable balance between the accuracy and the cost of computations. Table 2 is formulated after multiple runs of the developed simulation program using different time intervals. Table 2 represents the running time of the simulation program using different time intervals. Also, it represents the outputs of the maximum chamber pressure and muzzle velocity due to different time intervals.

Table 2: Time intervals, running time

Time Step (ms)	Running Time (s)	Maximum Chamber Pressure	Muzzle Velocity
1	0.43	281.7	882.6
0.1	0.50	332.8	911.7
0.01	1.13	338.8	914.2
0.001	8.73	339.4	914.5
0.0001	798.47	339.5	914.5

As can be seen form table 2, the time interval of 1 millisecond forms the starting point. At the time interval of 0.1 millisecond, the running time of the program is 0.5 of a second. At the time interval of 0.01 millisecond, the running time of the program is approximately 1.13 second. It can be noticed the readings of the maximum pressure and muzzle velocity significantly differed from the previous time interval. At the time interval of 0.001 millisecond, the running time of the program is approximately 8.73 seconds, which is a bit long. The readings of the maximum pressure and muzzle velocity not differed from the previous time interval. At the time interval of 0.0001 millisecond, the running time of the program is approximately 798.47seconds, which is unacceptable. However, there is almost no differences between the current readings and the readings of the previous time interval. As a result, the selected time interval that offers a great balance between the accuracy and the cost of computations is 0.001 millisecond.

The program is ready to be verified against RDM's IB simulation program. The following table shows the outputs of the developed and RDM's IB simulation program, respectively.

Table 3: RDM and developed program comparisons

155 mm Artillery System	RDM	Developed program	Deviation
Maximum Pressure (MPa)	339.8	339.4	-0.12
Time at Maximum Pressure (ms)	6.6	6.6	0.00
Muzzle Velocity (m/s)	916.0	914.5	-0.16
Spin Rate (rad/s)	1858.6	1835.4	-1.25
Projectile Exit time (ms)	15.7	15.7	0.00
Exits Pressure (MPa)	49.8	49.9	0.20
Wall Temperature (K)	651.0	676.2	3.87
Friction Loss (kJ)	946.8	946.5	-0.03

Table 3 demonstrates that the current simulation program is performing very well against RDM's IB simulation program. However, there is an extremely small error between both programs. The deviation can be referred to the rounding error and numerical method. The numerical method used in the RDM's IB simulation program is the pre-corrector Euler method. The deviation between both programs in projectile exit time and time at maximum pressure is zero. The deviation in maximum chamber pressure and muzzle velocity is 0. 12 and 0. 16 percent, respectively. The deviation in spin rate pressure and exits pressure is -1.25 and 0. 20 percent, respectively. The deviation in wall temperature is -0.03 percent.

Based on table 3, the developed simulation program seems quite accurate, mature, and consequently, performs well against the RDM's IB simulation program.

3.2.6 Stage three of LPM simulation program development

At this stage, the LPM is expanded. Three heat transfer variations, which were discussed in Sections 2.4 and 2.5, are lumped into the simulation program. The program is able to switch between the heat transfer variations conveniently. Figure 32 shows the flowchart of the LPM simulation program after the expansion.

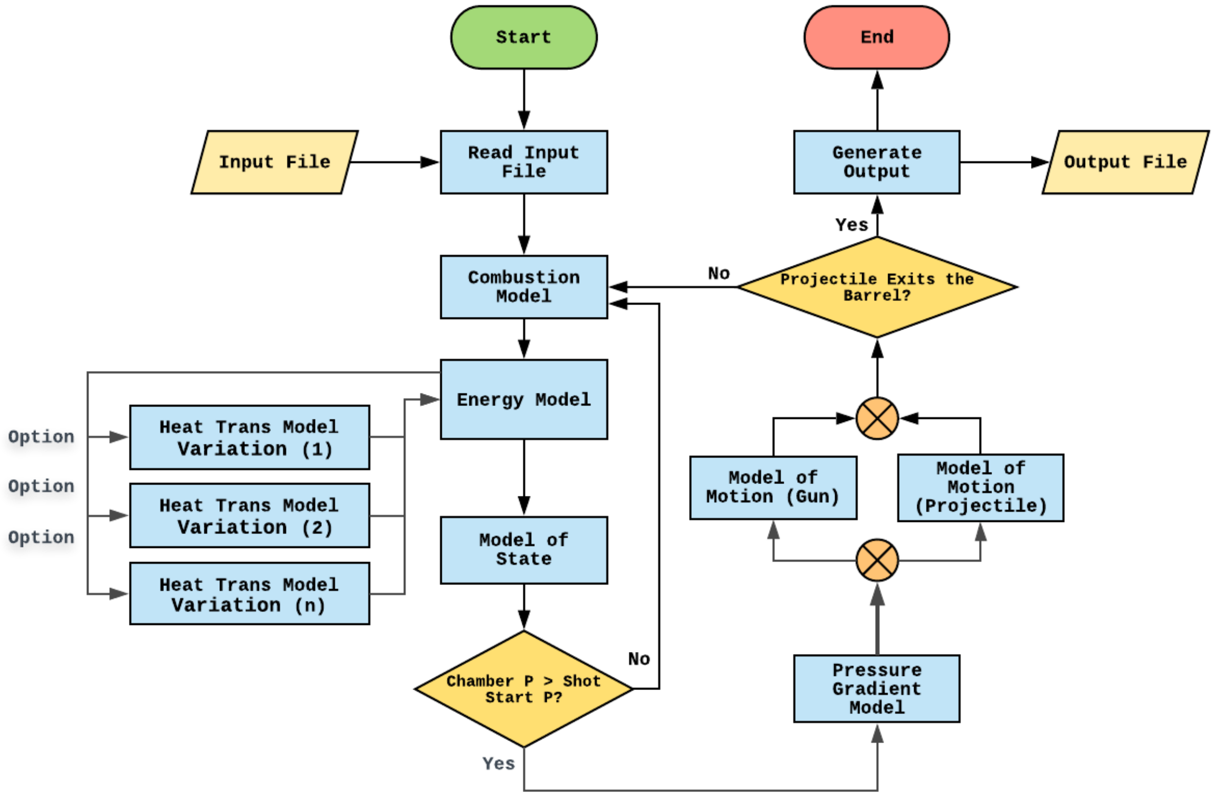

Figure 32: The flowchart of expanded version of LPM of IB

1. The program starts by reading all the inputs.
2. The combustion model calculates the generated gas mass due to propellant burning and the remaining solid mass of the propellant.
3. The option of the heat transfer model variation is checked via the program and is selected accordingly.
4. The energy model calculates the available energy in the propellant gas and passes it to the equation of state to calculate the space-mean pressure.
5. The program checks the space-mean pressure if it is greater than the shot start pressure or not.
6. If the space-mean pressure is still less than the shot start pressure, the program will loop until the condition is met.
7. After the condition is met, the space-mean pressure is passed to the pressure gradient model to calculate the excreted pressure on the projectile base and gun breech.
8. After that, the equation of motion solves the acceleration, velocity, and displacement of the projectile and gun.

9. The projectile state is checked via the program. If the projectile exits the muzzle, the outputs are generated and the program is terminated. However, if the projectile has not exited the muzzle, the program will loop until the condition is met.

3.2.6.1 Model verification

The expanded lumped parameter simulation program underwent one stage of verification. It is by visually examining the generated outputs of all variations of the heat transfer model, which is discussed in Sections 2.4 and 2.5, and making sure there are neither oscillations nor discontinuities in their outputs. The output variables of the heat transfer model, which have to be examined to ensure that the model is correctly implemented, are the following:

- Energy loss due to heat transfer, and
- Chamber wall temperature.

There are three possible variations that can be formulated using the heat transfer coefficients equations and chamber wall temperature equation, which are mentioned in Sections 2.4 and 2.5. The first variation is by using the convective heat transfer coefficient of STANAG 4367 and the one-dimensional equation of calculating the chamber wall temperature. Figure 33 represent the output curves of the first variation.

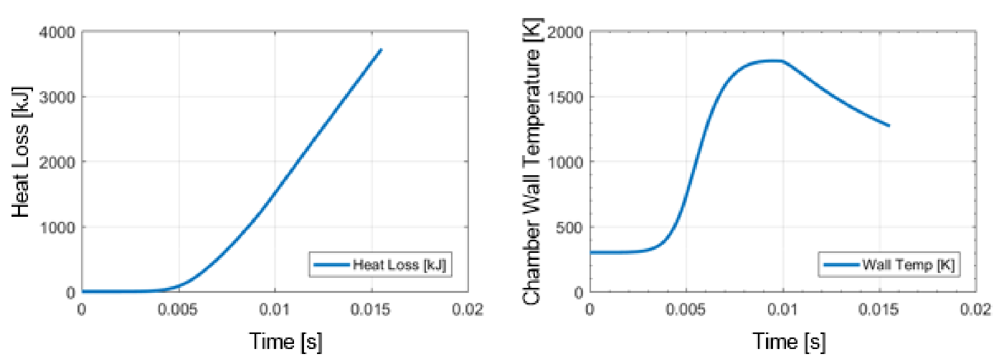

Figure 33: First variation of heat transfer model

The outputs of the first variation are free of any oscillations or discontinuities, which indicates that the variation is well-implemented. The second variation is formulated by using the convective heat transfer coefficient of Gough and the one-dimensional equation of calculating the chamber wall temperature. Figure 34 shows the outputs generated by the second variation.

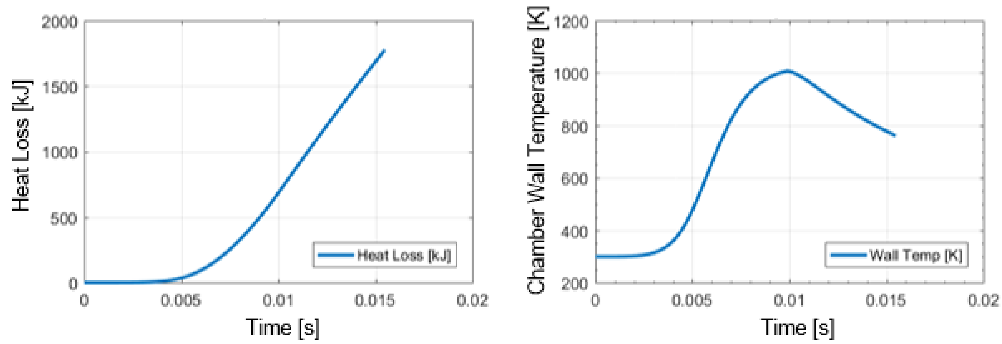

Figure 34: Second variation of heat transfer model

The outputs of the second variation are free of any oscillations or discontinuities, which indicates that the variation is correct and well-implemented. The third variation is formulated by using the coefficient of Lawton and the one-dimensional equation of calculating the chamber wall temperature. Figure 35 shows the outputs generated by the third variation.

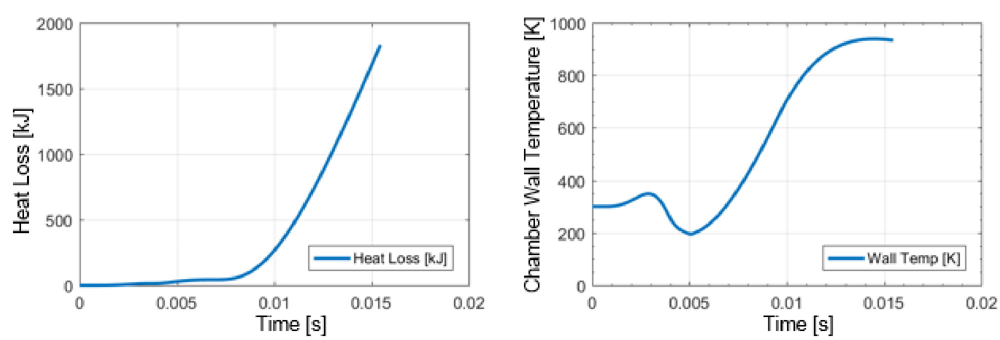

Figure 35: Third variation of heat transfer model

As can be seen, there are neither oscillations nor discontinuities in the third variation, which indicates that the variation is well-implemented.

It has been noticed that each variation of heat transfer model gives different temperature of the chamber wall and different amounts of lost energy due to heat transfer. Unfortunately, there is no measured data available to compare each model against. In the maximum chamber wall temperature, the difference between the first variation and the second variation is in the order of 75 percent, which is significant. The difference between the first variation and the third variation is approximately 84 percent. The difference between the second variation and the third variation is approximately -5 percent. Conversely, in the energy loss due to heat transfer, the difference between the first variation and the second variation is approximately 114 percent, which is significant. The difference between the first variation and the third variation is also in the order of 114 percent the difference between the second variation and the third variation is in the order of -2 percent.

The difference between the variations of the heat transfer model gives an indication that each variation will have a certain influence on the output of the LPM simulation program.

3.3 Conclusion

In this chapter, the simulation program was developed through three stages. The first stage was to build the simulation program of pneumatic gas gun. Then, the simulation program of pneumatic gas gun was expanded to be STANAG 4367 compliant by adding the combustion model as well as the pressure gradient model. During the last stage, the simulation program was expanded to include the three variations of the heat transfer model, which were discussed in Sections 2.4 and 2.5. The simulation program was verified against the interior ballistic simulation program of Rheinmetall Denel Munition (Pty) Ltd. Now, the simulation program is ready to be used to perform the investigation, which is to select the most suitable heat transfer model for the simulation of a 155 mm artillery system.

Chapter IV Modelling

4.1 Introduction

In the previous chapter, the interior ballistic simulation program, which serves the aim of this research, was developed and verified. In this chapter, the 155 mm artillery system, which is included in the investigation, will be briefly described. The investigation requires actual measured muzzle velocity and maximum chamber pressure of a 155 mm artillery system. Therefore, in this chapter, the process of obtaining the measured data is briefly explained. The 155 mm artillery system would be simulated multiple times using the developed interior ballistic simulation program. At each simulation, the variation of the heat transfer model would be alternated. The effect of each heat transfer variation on the simulated muzzle velocity and maximum chamber pressure would be observed. The simulated muzzle velocity and maximum chamber pressure of each simulation would be compared against measured values of the 155 mm artillery system as well as the simulated result with the STANAG 4367 heat transfer model. In this chapter, the most suitable heat transfer variation for simulating a 155 mm artillery system will be recommended and validated against different configuration of 155 mm artillery system.

4.2 155 mm artillery system

There are several configurations of the 155 mm artillery system. They mainly differ in their propellant charge mass and their barrel length. The 155 mm artillery system, which is used for the investigation, is known as Kingfisher. The barrel length is approximately 7 meters long. However, the chamber diameter has a slightly larger diameter than the bore. The chamber diameter is 175 mm. The system fires a projectile that weighs approximately 43 kg. The total weight of propellant loaded into its chamber is approximately 16 kg of progressive propellant. The propellant is known as M92, which is manufactured by RDM.

4.3 Data acquisition

Data acquisition is the process of measuring physical phenomenon using the data acquisition (DAQ) system. The DAQ system consists of sensors, a signal condoning device, and a computer system. The measurement of the physical phenomenon begins with sensors. Sensors sense any change in the physical phenomenon and convert it into measurable electrical signals that are readable by the DAQ device. Some sensors might require an extra circuitry to assists them with producing readable signals by the DAQ devise. National Instruments (2018) explains that, DAQ digitizes incoming analog signals so computers can interpret them. The DAQ device conditions the signal coming from the sensors by either amplification, attenuation, synchronizing, or others. Then, it hands it over to the computer system. The computer system is supported with an application software that gives the user the ability to acquire, analyze, and present the measured data (Instruments, 2018).

4.3.1 Instrumentations

The required data for this research is the muzzle velocity as well as the maximum chamber pressure of the 155 mm artillery system. To measure the maximum pressure, a piezoelectric pressure sensor is used. Piezoelectric pressure sensors consist of piezo sensors, which generate an electric charge that is proportional to the pressure applied (Agarwal, 2018). The piezoelectric pressure sensor is screwed within the breech.

The instrument that is used to measure the muzzle velocity of the projectile is the Doppler radar. The Doppler radar method is the only method to measure the muzzle velocity of a projectile of artillery systems. The Doppler radar system transmits a radar beam towards the moving projectile. Once the beam hits the moving projectile, it reflects to the radar system, which is received by an antenna. Based on the beam frequency, the velocity of the projectile can be calculated. The Doppler radar system is always located near the muzzle and points towards the firing direction (Hayden, 2018). The Doppler radar is also used to track the trajectory of the projectile for exterior ballistic applications.

4.3.2 Test setup

Figure 36 illustrates a typical test setup to measure the maximum chamber pressure, as well as the muzzle velocity of a 155 mm artillery system. The instruments that are involved in the test are the Doppler radar system to measure the muzzle velocity of the projectile, a piezoelectric pressure sensor to measure the maximum pressure of ballistic system, and a triggering device to trigger the other instruments to start measuring.

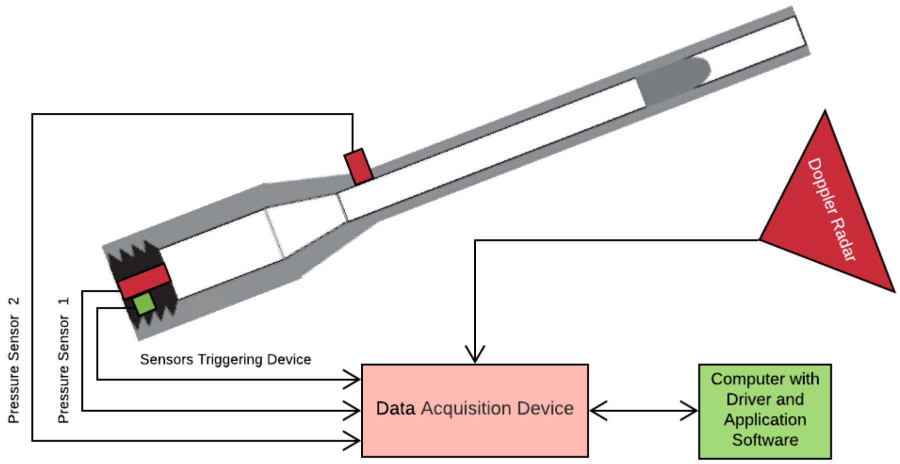

Figure 36: Test setup

During the test, the triggering device senses the striker impacting on the igniter. Thus, it gives the green light to the other instruments to start measuring. The pressure sensor starts measuring the chamber pressure throughout the interior ballistic cycle. As the projectile exits the muzzle, the Doppler radar will detect the projectile and lock onto it. Then, it measures the muzzle velocity of the projectile. The measured data would be send to the data acquisition device where it is amplified and transformed into readable data.

4.4 Data pre-processing

The data acquired from the test is raw data. Usually, raw data requires extra processing. The piezoelectric pressure sensor is integrated within the 155 mm artillery system. Thus, it experiences massive vibration during the ballistic cycle, which might introduce large amounts of noise to the signal. The noise has to be filtered out. Filtering the data is very critical. It centers on discovering the important patterns in the data while leaving out the noise. The main function of data filtering is to smooth the measured data and make it presentable, readable, and process-able. The Doppler radar system is an independent system. In other words, it does not experience massive vibrations caused by the 155 mm artillery system. As a result, its measurement does not need any further processing.

4.4.1 Data filtering

There are several filters that are used for data filtering. Moving average filter is the simplest one. It takes a sample (n) of data points at a time. Then, it takes the mean of those points to produce a single output point. As the sample (n) gets larger, the data becomes smoother. However, moving average is the least accurate filter because it assumes each point is equally weighted, thus, each point contributes equally to the total average. Sometimes, moving average smooths extreme values, which might be very important pieces of information. Conversely, weighted moving average (WMA) filter is always considered as a better option. WMA filters takes sample (n) of data points at a time and takes the mean of those to produce a single output point. However, it assumes each point is not equally weighted and the main point weighs the most. Thus, the main point significantly contributes to the total average. As a result, the extreme values within the data are not smoothed out. There are a few types of WMA filters, which are polynomial, exponential, and binomial WMA filters. The following figure shows the measured pressure curve after applying the binomial weighted moving average filter (Milton, 2018).

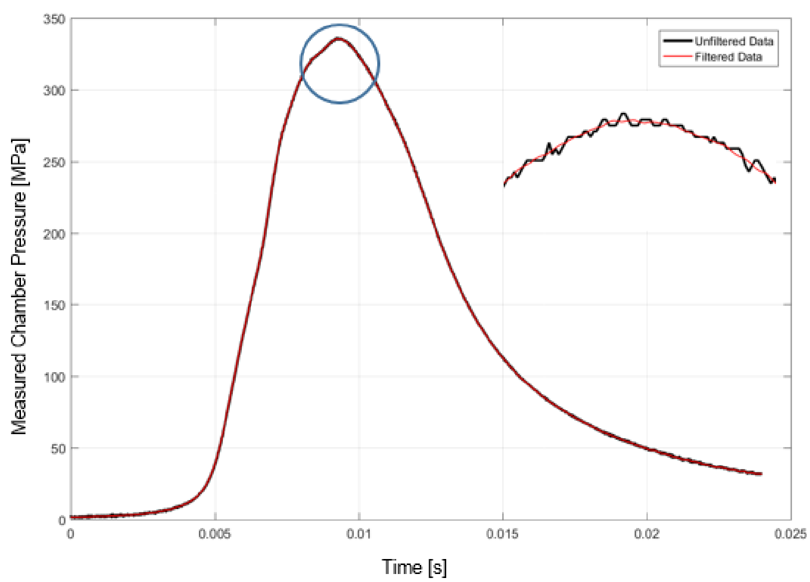

Figure 37: Measured pressure time curve

As can be seen, there is noise in the measured pressure curve. Figure 37 shows the measured curve before and after filtering. Table 4 represents the measured value of the maximum chamber pressure as well as the muzzle velocity of the 155 mm artillery system mentioned in Section 4.2.

Table 4: Measured data

	155 mm artillery system
Maximum Chamber Pressure (MPa)	348.0
Muzzle Velocity (m/s)	953.0

The measured maximum pressure of the 155 mm artillery system, mentioned in Section 4.2, is equal to 348 MPa. The measured muzzle velocity is 953 m/s.

4.5 The investigation

The 155 mm artillery system, which is mentioned in Section 4.2, is simulated using the developed LPM simulation program. The 155 mm artillery system would be simulated four times. The simulation sequence would be as follows:

1. During the first simulation, the simulation program would be adjusted to match the LPM of STANAG 4367. Thus, the used heat transfer model would be that of STANAG 4367.

2. During the second simulation, the simulation program would be adjusted to use the first variation of the heat transfer model, which utilizes the convective heat transfer coefficient of STANAG 4367 and the one-dimensional equation of calculating the chamber wall temperature.

3. During the third simulation, the simulation program would be adjusted to use the second variation of the heat transfer model, which utilizes the convective heat transfer coefficient of Gough and the one-dimensional equation of calculating the chamber wall temperature.

4. During the fourth simulation, the simulation program would be adjusted to use the third variation of heat transfer model, which utilizes the coefficient of Lawton and the one-dimensional equation of calculating the chamber wall temperature.

The effects of each variation of the heat transfer model on the simulated results would be observed. All the variation of the heat transfer model would be compared to the STANAG 4367 heat transfer model and to actual measured muzzle velocity and maximum pressure of a 155 mm artillery system.

4.5.1 Maximum chamber pressure

Figure 38 below represents the predicted maximum chamber pressure generated by the developed simulation program using all variations of the heat transfer model including the heat transfer model of STANAG 4367. The vertical axis represent the chamber maximum pressure. The horizontal axis represent the different variations of heat transfer models. The red line reflects the maximum pressure, which is 348 MPa, of the simulated system.

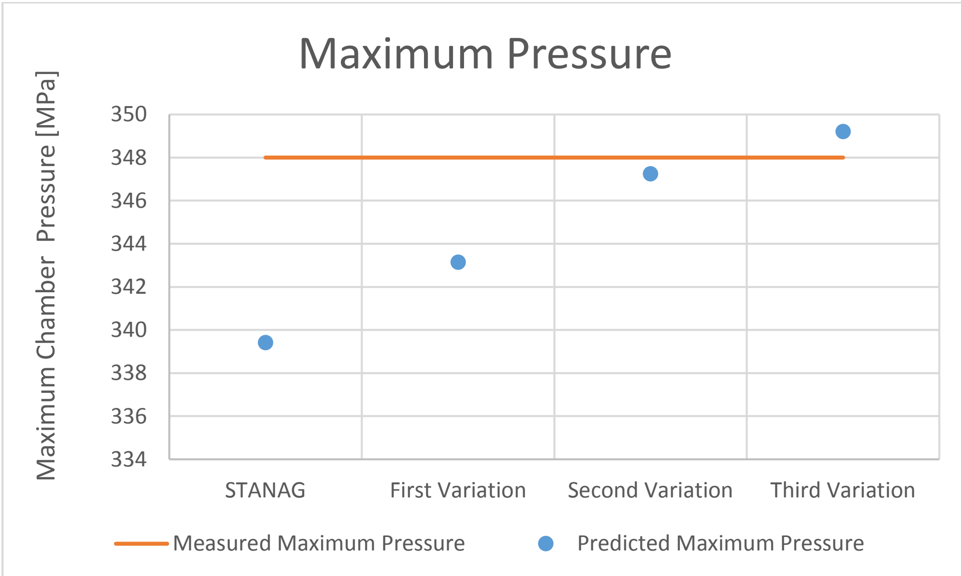

Figure 38: Predicted and measured maximum pressure of 155 mm artillery system

As can be seen, the gap between the LPM of STANAG 4367 and the measured value is relatively significant. The deviation is approximately -2.5 percent (-10.5 MPa). By just changing the chamber wall temperature equation of STANAG 4367 to the proposed one-dimensional equation, the prediction of the LPM improved. The first variation predicts the maximum pressure of a 155 mm artillery system with a deviation of -1.4 percent (-5 MPa). When the second variation is utilized, the LPM gives a better prediction with a deviation that is approximately -0.2 percent (-0.7 MPa). Conversely, when the third variation of the heat transfer model is utilized, the LPM slightly over predicts the maximum chamber pressure of a 155 mm artillery system with a deviation that is approximately 0.4 percent (1.2 MPa).

4.5.2 Muzzle velocity

Figure 39 below represents the predicted muzzle velocity generated by the developed simulation program using all variations of the heat transfer model including the heat transfer model of STANAG 4367. The vertical axis represent the muzzle velocity. The horizontal axis represent the different variations of heat transfer models. The red line reflects muzzle velocity, which is 953 m/s, of the simulated system.

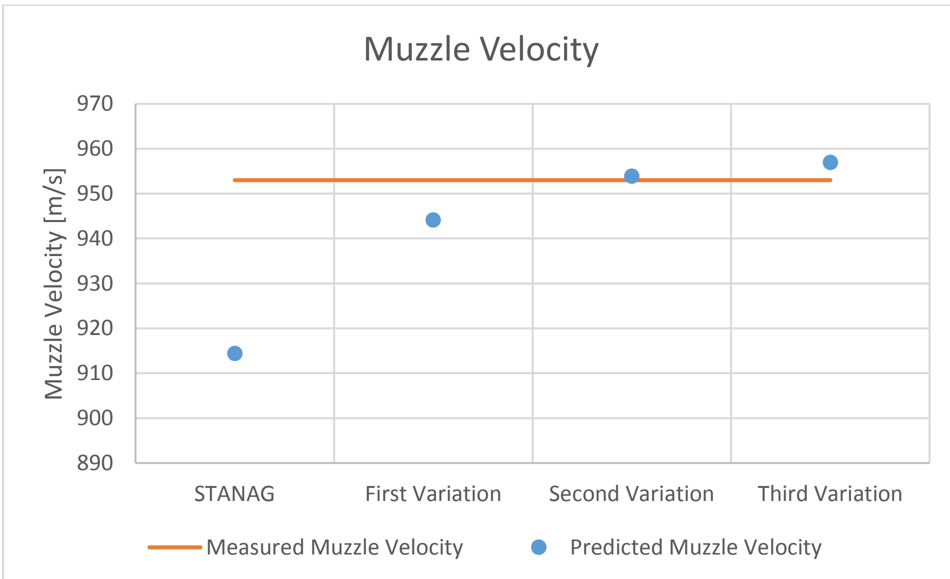

Figure 39: Predicted and measured muzzle velocity of 155 mm artillery system

As illustrated, the gap between the lumped parameter of STANAG 4367 and the measured muzzle velocity is relatively significant. The deviation is approximately -4 percent (-40 m/s). By just changing the chamber wall temperature equation of STANAG 4367 to the proposed one-dimensional equation, the prediction of the LPM program improved. The first variation predicts the muzzle velocity of a 155 mm artillery system with a deviation of -0.9 percent (-10 m/s). When the second variation is utilized, the LPM gives a better prediction with a deviation that is approximately -0.09 percent (0.9 m/s). Conversely, when the third variation is utilized, the program slightly predicts the muzzle velocity of a 155 mm artillery system with a deviation that is approximately 0.4 percent.

4.5.3 Overall error

The heat transfer model significantly effects the predictions of the lumped parameter mode of interior ballistics. The selection of the most suitable heat transfer variation is based on the overall deviation of the LPM. Thus, overall deviation is the parameter for selecting the best variation of heat transfer model for simulating the 155 mm artillery system. The overall deviation is the average deviation of the muzzle velocity and maximum pressure. Figure 40 illustrates the average deviation of the LPM of interior ballistics using all different variations of heat transfer model including STANAG 4367. If the deviation is positive, the LPM over predicted the performance of the 155 mm artillery system. If the overall deviation is negative, it means the LPM under predicted the performance of the 155 mm artillery system.

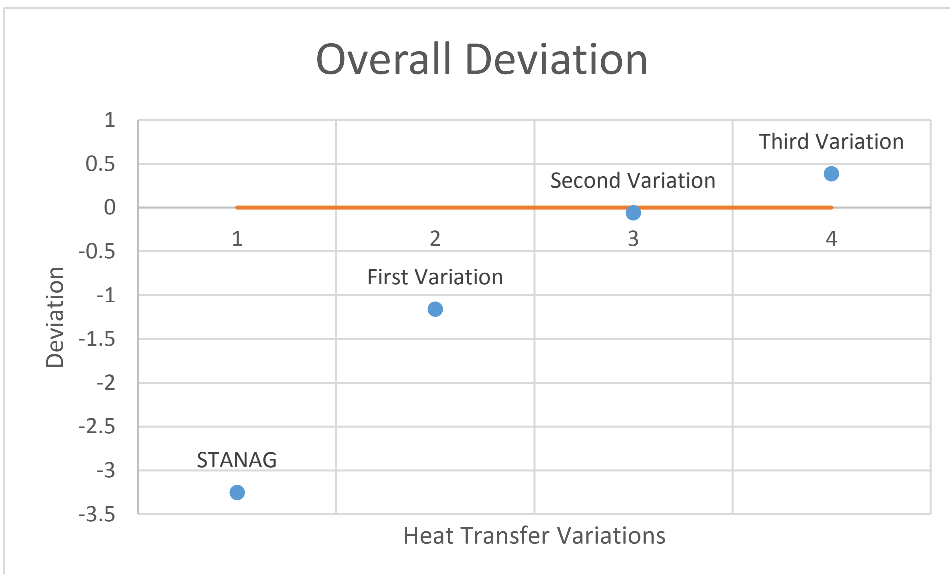

Figure 40: Overall deviation of the LPM using different variations

The overall deviation between the LPM of STANAG 4367 and the measured value is approximately -3.3 percent. By just changing the chamber wall temperature equation of STANAG 4367 to the proposed one-dimensional equation, the deviation of the LPM program improved to be around -1 percent. When the second variation is utilized, the overall deviation of the LPM is approximately - 0.06 percent. When the third variation is utilized, the overall deviation of the LPM is approximately -0.5 percent. To conclude, the most suitable variation of the heat transfer model to be utilized for the LPM of interior ballistics is the second variation of the heat transfer model.

4.6 Model Validation:

The second variation of the heat transfer model was recommended as the most suitable variation to be used in the LPM of interior ballistics when simulating a 155 mm artillery system. Now, the LPM with the second variation of heat transfer model is going to be validated against different configurations of a 155 mm artillery system. In addition to that, the first variation will also be included in the validation to validate the proposed one-dimensional equation of the chamber wall temperature as a better alternative to chamber wall temperature equation of STANAG 4367.

4.6.1 155 mm artillery system second configuration

The second configuration of a 155 mm artillery system is known as G5. The barrel length is approximately 6 meters long. The chamber diameter has a slightly larger diameter than the bore. The chamber diameter is 175 mm. The system fires a projectile that weighs approximately 46 kg. The total weight of propellant loaded into its chamber is approximately 15 kg of progressive propellant. The propellant known as M64, which is manufactured by RDM. The measured maximum chamber pressure and muzzle velocity of the second configuration of the 155 mm artillery system are 378 MPa and 918 m/s respectively.

4.6.2 Maximum pressure

Figure 41 below represents the predicted maximum chamber pressure generated by the developed simulation program using the first and second variations of the heat transfer model including the heat transfer model of STANAG 4367. The vertical axis represent the chamber maximum pressure. The horizontal axis represent the different variations of heat transfer models. The red line reflects maximum pressure, which is 378 MPa, of the simulated system.

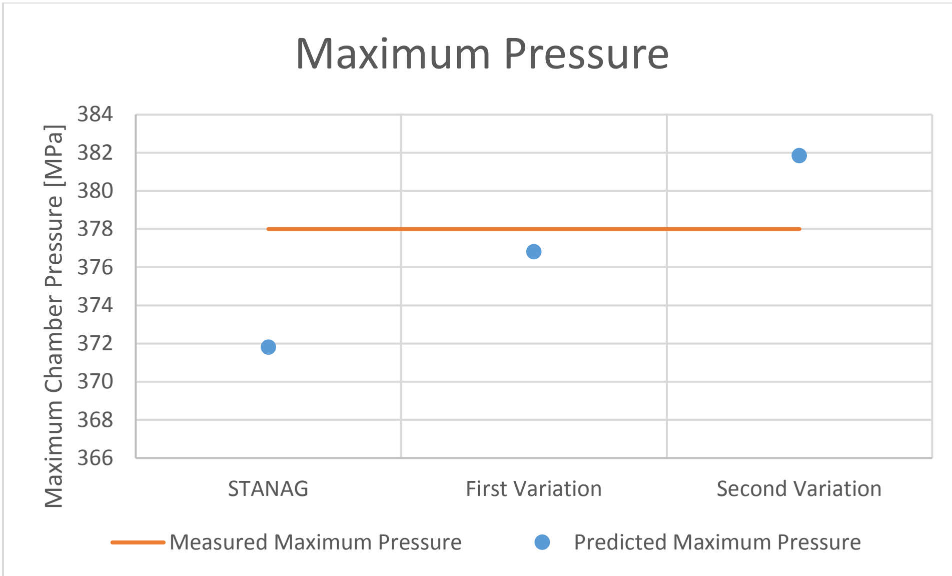

Figure 41: Predicted and measured maximum pressure of 155 mm artillery system

As can be seen, the gap between the LPM of STANAG 4367 and the measured value is still significant. The deviation is approximately -1.6 percent (-6 MPa). By just changing the chamber wall temperature equation of STANAG 4367 to the proposed one-dimensional equation, the prediction of the LPM improved. The first variation predicts the maximum pressure of the 155 mm artillery system with a deviation of -0.3 percent (-1.2 MPa). When the second variation is utilized, the LPM slightly over predicts the maximum chamber pressure of the 155 mm artillery system with a deviation that is approximately 1 percent (3.8 MPa).

4.6.3 Muzzle velocity

Figure 42 below represents the predicted muzzle velocity generated by the developed simulation program using the first and second variations of the heat transfer model including the heat transfer model of STANAG 4367. The vertical axis represent the muzzle velocity. The horizontal axis represent the different variations of heat transfer models. The red line reflects muzzle velocity, which is 918 MPa, of the simulated system.

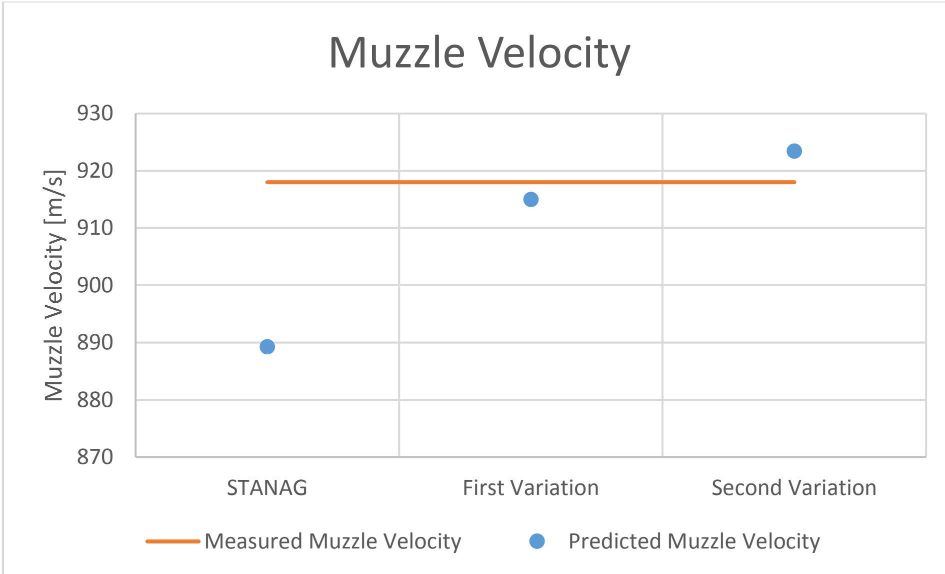

Figure 42: Predicted and measured maximum pressure of 155 mm artillery system

As can be seen, the gap between the lumped parameter of STANAG 4367 and the measured muzzle velocity is relatively significant. The deviation is approximately -3 percent (-28 m/s). By just changing the chamber wall temperature equation of STANAG 4367 to the proposed one-dimensional equation, the prediction of the LPM program improved. The first variation predicts the muzzle velocity of the 155 mm artillery system with a deviation of -0.3 percent (-3 m/s). When the second variation is utilized, the program slightly over predicts the muzzle velocity of the 155 mm artillery system with a deviation that is approximately 0.6 percent (5 m/s).

4.6.4 Overall deviation

Figure 43 illustrates the average deviation of the LPM of interior ballistics using the first and second variations of heat transfer model including STANAG 4367.

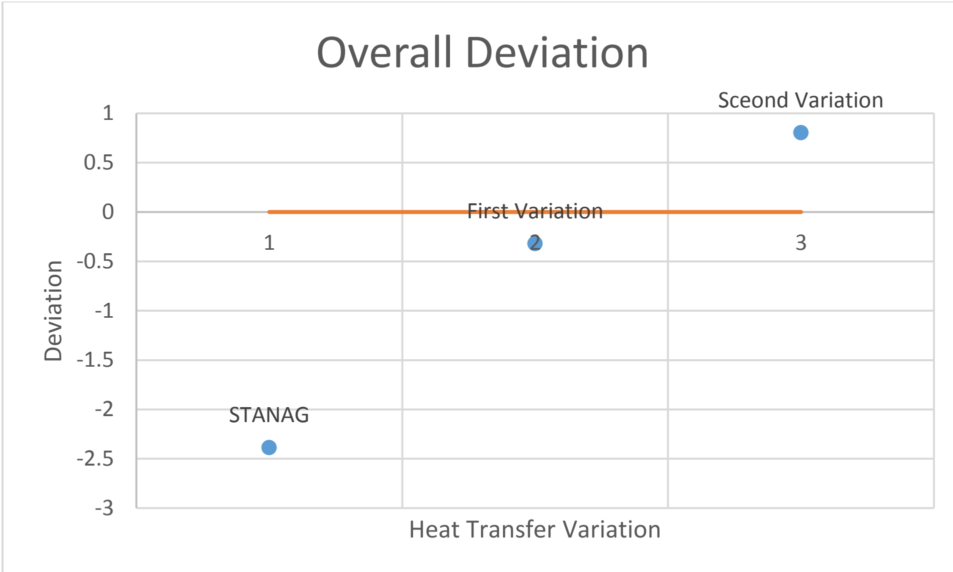

Figure 43: Overall deviation of the LPM using different variations

As can be seen, the overall deviation between the LPM of STANAG 4367 and the measured values is approximately -2.4 percent. By just changing the chamber wall temperature equation of STANAG 4367 to the proposed one-dimensional equation, the deviation of the LPM program improved to be -0.3 percent. When the second variation is utilized, the overall deviation of the LPM is approximately 0.8 percent. To conclude, when the first and second variations of the heat transfer model are utilized in the LPM, it becomes more accurate than the LPM of STANAG 4367.

4.7 Conclusion

In this chapter, there was a brief explanation on the 155 mm artillery system that was included in the investigation. Also, there was a brief explanation about data acquisition and processing. The 155 mm artillery system was simulated four times by the developed interior ballistic simulation program. At each time, the program was adjusted to a LPM of interior ballistic with alternative variations of the heat transfer model. The main purpose of the investigation is to recommend the most suitable heat transfer model variation to be used when simulating the 155 mm artillery system. It has been found that, the second variation of heat transfer model, which utilizes the convective heat transfer coefficient of Gough and the one-dimensional equation of calculating the chamber wall temperature, is the most suitable variation to be used when simulating a 155 mm artillery system. In addition to that, the one-dimensional equation of calculating the chamber wall temperature is a better alternative to the chamber wall temperature equation of STANAG 4367.

The first and second variations of heat transfer models were used in the LPM of interior ballistics and were validated against different configurations of a 155 mm artillery system. It has been found that the LPM with both variations outperformed the LPM of STANAG 4367 in terms of accuracy. As a result, the first and second variations of the heat transfer models are validated to be used as alternatives to the heat transfer model of STANAG 4367 when simulating a 155 mm artillery system.

Chapter V Conclusion and Recommendation

5.1 Research overview

In Chapter 1, the essential background to the problem was provided. The problem was that when the LPM of STANAG 4367 is used to simulate the 155 mm artillery system, it gives predictions with relatively large deviations. The ballistician consequently loses confidence in his/her model. The problem was detected to be in the heat transfer model in STANAG 4367. The aim of the research was provided, which is to find a better alternative heat transfer model that when used in the LPM to simulate a 155 mm artillery system, it would give a prediction with smaller deviations.

In Chapter 2, all the essential background to the LPM of STANAG 4367 was provided. Furthermore, alternative heat transfer models were provided. However, to find the most suitable heat transfer model, a simulation program of interior ballistics had to be developed.

In Chapter 3, the simulation program, which was needed for the investigation, was developed. Furthermore, the simulation program was verified against the simulation program of RDM. The heat transfer models, which were provided in Sections 2.4 and 2.5, were lumped into the simulation program and verified by making sure there were neither oscillations nor discontinuities in their variables.

In Chapter 4, the 155 mm artillery system was simulated via the developed simulation program using all the variations of the heat transfer model. All the simulation results were compared to the actual measured data of the 155 mm artillery system. The heat transfer model that assists the LPM of interior ballistics to give predictions with small variations were recommended.

In Chapter 5, a different configuration of a 155 mm artillery system was briefly described. The first and second variations of the heat transfer models were included in Chapter 5 for validation. These heat transfer models were validated against different configurations of the 155 mm artillery system.

The first and second variations of heat transfer model proofed to be better alternatives to the heat transfer model of STANAG 4367.

5.2 Conclusion

The research aimed to provide a better alternative to the heat transfer model of STANAG 4367, in order to improve the accuracy of the LPM when simulating a 155 mm artillery system. Also, it aimed to provide an interior ballistic simulation program that is practical for interior ballistic applications such charge mass determination.

The heat transfer model that improved the accuracy of the LPM when simulating a 155 mm artillery system is the second variation, which was proposed in Sections 2.4 and 2.5. The second variation of heat transfer model utilizes the one-dimensional equation for the chamber wall temperature and convective heat transfer coefficient of Gough. Furthermore, when the one-dimensional equation of the chamber wall was coupled with LPM of STANAG 4367, the deviations of the muzzle velocity and maximum pressure predictions were smaller. The research also aimed to provide guidelines for interior ballistic simulation procedures when the ballistic system has a constant or variable gun wall thickness. The guideline is outlined in the recommendation section.

5.3 Recommendation

1. When the 155 mm artillery system is simulated using the LPM of STANAG 4367, it is recommended to change the equation of chamber wall temperature to the one-dimensional equation, which was proposed in Section 2.4. It is also recommended to utilize the convective heat transfer coefficient of Gough, which was also proposed in Section 2.4.

2. If any ballistics system is simulated using the LPM of STANAG 4367 and that ballistics system has non-nominal chamber wall thickness, it is recommended to change the equation of chamber wall temperature of STANAG 4367 to the one-dimensional equation, which was proposed in Section 2.4.

3. When the simulated ballistic system has a nominal wall thickness, such as mortar systems, it is recommended to use the LPM of STANAG 4367 as it gives accurate predictions.

5.4 Further Study

A 155 mm artillery system shall be simulated using the LPM with the new variations of heat transfer models and the one-dimensional model of interior ballistic. The predictions of both models shall be compared to the measured maximum chamber pressure and muzzle velocity. Both models shall be compared against each other in term of accuracy, advantages, and disadvantages.

List of References

Jedlicka, L., & Beer, S. (2007). PRESSURE DISTRIBUTION IN THE SPACE BEHIND A PROJECTILE. *Advances in MT*, 35-48.

Agarwal, T. (2018, 12 09). *A Brief Introduction to Piezoelectric Sensor Switch And its Working Procedure*. Retrieved from Edgefx: https://www.edgefx.in/piezoelectric-sensor-switch-working/

Antonie, D. (2013). Modeling of Constant Volume Combustion of Propellants for Artillery Weapons. *Termotehnica* , 121-125.

Bingue, D. E. (2018, 12 08). *Papers.* Retrieved from Conferences.omputer: http://conferences.computer.org/stc/2014/papers/5034a024.pdf

Carlucci, D. J. (2007). *BALLISTICS THEORY AND DESIGN OF GUNS AND AMMUNITION.* London: Taylor & Francis Group, LLC.

Consultancy, F. N. (2018, 12 11). *WEAPONS SYSTEMS-INTERNAL BALLISTICS SOFTWARE FNGUN*. Retrieved from Frazer-Nash Consultancy: https://www.fnc.co.uk/markets/defence/weapons-systems/internal-ballistics-software-fngun.aspx

Dyckmans, G. (2015). Fundamentals of Ballistics. Belgium. Retrieved from https://e-ballistics.com/author.html

GICHD. (2018, 11 21). *Characterisationexplosiveweapons*. Retrieved from GICHD: http://characterisationexplosiveweapons.org/studies/annex-c-81-82-120-mm-mortars/

Gough, P. (1983). *Two-dimentional, two phase modelling of multi-incrementa; bagged artill.* ARBRL.

Gronheim, A. (2000). *Thermodynamic Interior Ballistic Model with Global Parameters 2nd ed.* Brussels: MAS and BMS.

Gunpowder. (2019, 03 1). *Gunpowder*. Retrieved from Wikipedia, the free encyclopedia: https://en.wikipedia.org/wiki/Gunpowder

Hansen, E. C., & Heiney, O. K. (1987). *Pressure And Gas Flow Gradients Behind The Projectile During The Interior Ballistic Cycle.* Florida: University of Florida.

Hayden, R. (2018, 12 09). *Doppler Radar Method*. Retrieved from Exteriorballistics.com: http://www.exteriorballistics.com/ebexplained/5th/233.cfm

Instruments, N. (2018, 12 09). *Products*. Retrieved from National Instruments: http://www.ni.com/data-acquisition/what-is/

Johnston, I. A. (2005). *The Noble-Abel Equation of State: Thermodynamic Derivations for Ballistics Modelling.* Edinburgh: Defence Science and Technology Organisation.

Johnston, I. A. (2005). *Understanding and Predicting Gun Barrel Erosion.* Edinburgh: Defence Science and Technology Organisation.

Kubota, N. (2007). *Propellants and Explosives Thermochemical Aspects of Combustion.* Weinheim: WILEY-VCH Verlag GmbH & Co. KGaA.

Milton, A. (2018, 12 31). *Simple, Exponential and Weighted Moving Averages*. Retrieved from the balance: https://www.thebalance.com/simple-exponential-and-weighted-moving-averages-1031196

Moreno, J. A. (2009). *Thermodynamic Interior Ballistic Model With Global Parameters.* NATO Standardization Agency.

Morrison, W. F., & Wren, G. P. (1993). *The Application of Lagrange and Pidduck-Kent Gradient Models to Guns Using Low Molecular Weight Gases.* U.S. Army Research Laboratory.

Press, W. H. (2002). *Numerical Recipes in C.* Cambridge: Press Syndicate.

Russell, M. S. (2009). *The Chemistry of Fireworks.* Cambridge: The Royal Society of Chemistry.

Schabort, V. (2016). *RDM Internal Ballistic.* Somerset West: RDM.

Singh, S. (2009). *Hand Book of Mechanical Engineering.* S Chand.